Review

An overview of 2D metal sulfides and carbides as Na host materials for Na-ion batteries

Javed Rehman [a,b,*], Shiru Lin [c,d,*], Mehwish K. Butt [e], Xiaofeng Fan [f], Tamer Khattab [g], Khaled A. Elsayed [h], Mohamed F. Shibl [i,*]

[a] State Key Laboratory of Metastable Materials Science and Technology, and School of Materials Science and Engineering, Yanshan University, Qinhuangdao 066004, China
[b] Department of Physics, Baluchistan University of Information Technology, Engineering and Management Sciences (BUITEMS), Quetta, Baluchistan 87300, Pakistan
[c] School of Physics and Electronic Information, Yan'an University, Yan'an 716000, China
[d] Division of Chemistry and Biochemistry, Texas Woman's University, Denton, TX 76204, USA
[e] Shaanxi Key Laboratory of Condensed Matter Structures and Properties and MOE Key Laboratory of Materials Physics and Chemistry under Extraordinary Conditions, School of Physical Science and Technology, Northwestern Polytechnical University, Xi'an 710072, China
[f] Key Laboratory of Automobile Materials (Jilin University), Ministry of Education, and College of Materials Science and Engineering, Jilin University, Changchun 130012, China
[g] Electrical Engineering, Qatar University, 2713 Doha, Qatar
[h] Department of Basic Engineering Sciences, College of Engineering, Imam Abdulrahman Bin Faisal University, P.O. Box 1982, Dammam 31451, Saudi Arabia
[i] Renewable Energy Program, Center for Sustainable Development, College of Arts and Sciences, Qatar University, 2713 Doha, Qatar

ARTICLE INFO

ABSTRACT

Both sodium-ion batteries (SIBs) and lithium-ion batteries (LIBs) operate on a similar principle and are striking for energy storage purposes. Although some electrode materials adapt favorably to LIBs, they are not pertinent for SIBs systems because Na^+ (0.98 Å) has a significantly bigger diameter as compared to Li^+ (0.69 Å). The use of two-dimensional (2D) materials as anodes for SIBs has established tremendous advancement in the last decade through their exceptional 2D layered structure, infinite planar lengths, and highly disclosed active sites. 2D materials assist the current SIB anode materials as profitable successors. To resolve the energy storage crisis, superior quality anode materials are essential for rechargeable next-generation SIBs. Among all anode materials, layered metal sulfides (MSs) and metal carbides (MCs) are the promising host anodes for SIBs because of their substantial capacity and impressive redox reversibility. The distinctive structures of 2D MCs and MSs provide an innovative era to surmount the challenges in anode materials like structural collapse, volume change, small storage capacity, and confined phase variation. The layered structure and large surface area provide substantial potential for intercalating and hosting more Na ions, thus maximizing the storage capacity.

This review delineates some influential 2D MCs and MSs for anodic uses. In this review, we analyze theoretical and experimental techniques for scrutinizing predicted anode materials, electronic characteristics, and electrochemical performances, and they are reported to be beneficial for SIBs. Furthermore, the future perspective and the material design are described. The light shaded on the 2D MCs and MSs is anticipated to identify new anode materials for SIBs.

1. Introduction

Worldwide energy storage has turned into a critical issue for human survival. Current societies dependence on fossil fuels is being extremely impacted by huge fuel prices, pollution, global warming, and geopolitical concerns. These concerns can be minimized by promoting advanced storage technologies and energy resources. The progress of large-scale energy storage systems with substantial capacities, low prices, superior energy densities, and outstanding performance has captivated increasing deliberation during the last few years [1–6]. Li-ion batteries (LIBs) have offered marvelous opportunities and challenges in the energy storage area over two decades. Since the 1990 s LIBs have been

commercialized and prevailed in the market because they store clean energy and provide a constant power supply [7–10]. Moreover, LIBs have been applied in mobile electronics and transportation. However, the current LIBs confront hindrances such as capacity, effectiveness cost, and safety [11–16]. These challenges alleviate their use in further applications. In light of the insufficient resources of Li in the earth's crust (0.0017 wt%) [17,18], an alternative storage system must be developed for next-generation energy storage. The primary objective is to minimize these obstacles by breakthrough advanced storage technologies and sustainable energy resources.

In recent years, it has been noticed that SIBs have emerged as promising energy storage technology because of the rich resources of Na (2.36 wt%) [19–25]. Owing to their different ionic radii (0.76 Å for Li and 1.02 Å for Na), some anode materials can barely suit SIBs. For instance, graphite, the most customarily utilized anode material for LIBs, merely possess an insufficient capacity (35 mAh g^{-1}) for the SIBs [26]. Thus, high-capacity anode materials are desired for SIBs with a fast charge/discharge mechanism. Thanks to their exotic mechanical, electrical, and optical characteristics, 2D materials have gained tremendous interest in flexible nanoelectronics, photonics, and energy storage devices [27–30]. Since graphene was explored, the class of 2D materials has developed into metal oxides, sulfides, h-BN, MXenes, carbides, and phosphides [31–36]. 2D materials possess similar inherent benefits due to their enormous surface area and high mechanical strength [37–41]. However, the development of 2D anodes for SIBs still faces several obstacles, such as challenging synthesis strategies and unclear electrochemical processes [42–46].

Among 2D materials, metal sulfides (MSs) with layered structures and large surface areas show small volume variation and enhanced mechanical stability. The discharge product of MSs, such as Na$_2$S, endows high conductivity rather than metal oxides, such as Na$_2$O. In addition, the M–S bond is much stronger than the M–O bond, which concludes that MSs could be kinetically promising for conversion reactions. MSs have been widely applied to energy storage systems, including solar cells, metal-ion batteries, and supercapacitors [47–52]. Owing to the comparatively extensive research studies on the usage of metal sulfides as LIBs anodes, the possible applications of transition metal sulfides (TMSs) as high-performance SIB electrodes were also taken due to their electrochemical resemblances. TMSs illustrate high sodiation capacities because of their open-layered configurations, small volume variations, enhanced mechanical staility and the ability to execute conversion and alloying reactions, which makes them superior to analogously layered-structured carbonaceous materials [53–55]. Additionally, TMSs show values of higher ionic/electronic conductivities than those of numerous high-potential materials such as metal oxides and phosphides. This unique combination of multi-faceted structural benefits has thus attracted significant attention from the research community in addressing the stringent ionic needs to assist the transport characteristics and storage of sodium ions (Na$^+$ or Na-ions) [56–59].

On the other hand, the surfaces of 2D metal carbides (MCs) or MXenes are hydrophilic because of the terminated groups, including fluorine, hydroxyl, and oxygen. Owing to their ease of processing and low stabilization requirements, they can be suitable for thin films, devices, and coatings [60–62]. These materials exhibit exceptional properties for water splitting and triboelectric nanogenerators. They are also useful for batteries, supercapacitors, electromagnetic interference shielding, and capacitive desalination [63–71]. Specifically, the intercalation of Li$^+$ ions into MXenes could reach a steady-state capacity. Additionally, MXenes possess high-rate capability and high storage capacity as compared to carbon owing to the fast diffusion of Li and Na ions on their surfaces [72–76]. However, some challenges faced by these 2D materials can be fixed such as the reaction of discharge products with the electrolyte by separating the electrolytes and electrodes. The huge amount of Na$^+$ ions can take part in the chemical reaction and participate in large volume alterations. This problem could be solved by introducing a protective layer on the surface. Some 2D materials demonstrate poor reversibility after discharging due to the alloying and conversion reactions, ultimately leading to poor rate performance. The issues could be resolved by the addition of nanostructure design, voltage range selection, electrolyte optimization, and carbon modifications.

Herein, we encapsulate the recent advancement, computational methodologies, experimental validation, and electrochemical behavior of single-layer MSs and MCs as host materials for SIBs. This review paper outlines and discusses thoroughly the exciting advances of 2D materials used in SIBs. This contribution sheds light on the mechanism of 2D MSs and MCs in SIBs using both experimental analysis and first-principles calculations. The focus is to elaborate on the surface energy of Na-adsorbed and diffused on 2D metal sulfides and carbides. An in-depth study has been conducted on the correlation between structure and electrochemical performance. Last but not least, we discuss the conclusions and prospects of enhancing the sodium storage performance of such 2D materials.

2. The nature of SIBs

Similar to LIBs, SIBs consist of an anode, cathode, separator, and electrolyte [77]. A sodiation process involves Na$^+$ intercalating across the cathode and diffusing via the electrolyte to reduce the anode electrochemically. The thermodynamically adverse charging mechanism needs an external force to start the reverse reaction. It is governed by increasing the anode potential until the cell obtains the upper voltage limit. In the discharging process, the reverse reaction occurs, which is thermodynamically favorable [78]. A battery's driving force can be established based on the Gibbs free energy change between the reactants and products, as denoted by equation (i)

$$\Delta G_{rxn}^o = \sum \Delta G_f^o(\text{products}) - \sum \Delta G_f^o(\text{reactants}) \qquad (1)$$

The working span of a battery is defined as the difference between the energy of the highest occupied molecular orbital (HOMO) and the lowest unoccupied molecular orbital (LUMO) of the electrolyte. Decomposition of the electrolyte will occur if the anode potential (μ_a) is greater than the LUMO. A passivation layer is a self-formed resistive thin layer assembled due to the chemical reaction between the anode and the electrolyte. An energy barrier will happen to migrate ions from the electrolyte HOMO to the cathode, assuming that the potential of the cathode (μ_c) is smaller than the HOMO. Thus, to stabilize the battery, the electrodes need the potential to operate within the working window of the electrolyte (Fig. 1). Therefore, the open-circuit voltage (OCV, shown as V_{OC}) is restricted to the equation.

$$eV_{OC} = \mu_a - \mu_c \qquad (2)$$

and

$$\mu_a - \mu_c = E_g \qquad (3)$$

where E_g is the energy difference between the HOMO and the LUMO of the liquid electrolyte and e denotes the electron charge magnitude. The μ_a and μ_c characterize the electrochemical potentials of the anode and the cathode, correspondingly.

There are three major reasons why SIB will be a favorable replacement for LIBs. Firstly, sodium is a highly abundant element in the earth's crust, while lithium is comparatively scarce. Secondly, the electrode potential of sodium is stable and appropriate compared with lithium. Thirdly, the costly transition metals such as Co and Ni, commonly utilized in the LIB cathodes, can be substituted by elements with lower cost in SIBs [79,80] such as Mn and Fe. However, it is commonly believed that the Na-ion illustrates sluggish diffusion kinetics compared to the Li-ion because of its bigger radius. Therefore, sodium compounds provide many opportunities for surmounting the challenges arising from their large chemical space.

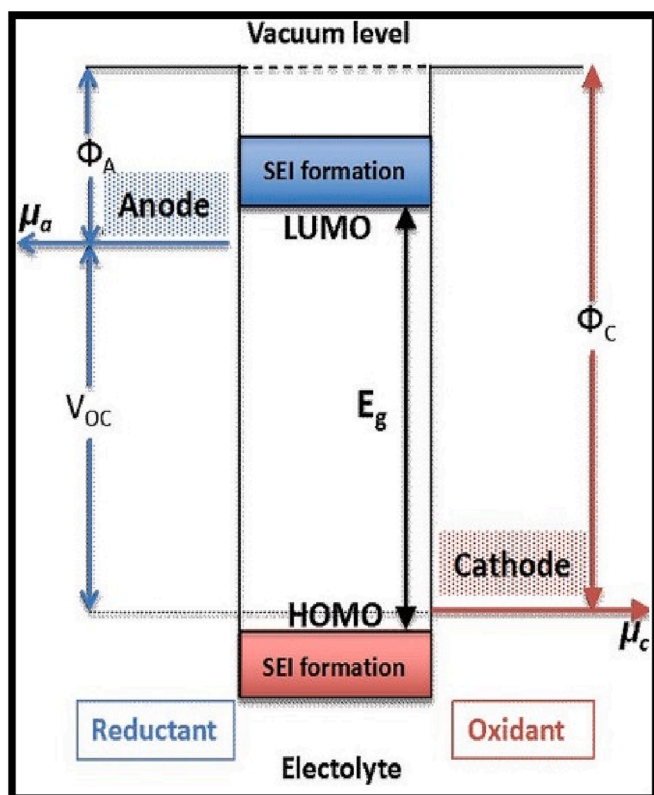On the other side, due to their larger ionic radius of Na$^+$ (55 %

Fig. 1. Schematic illustration of non-aqueous SIBs. The cathode and anode work functions are denoted by Φ_C and Φ_A, respectively. E_g is the energy gap between the HOMO and the LUMO. SEI layer will be formed if $\mu_a >$ LUMO and/or $\mu_c <$ HOMO [86].

greater) than Li$^+$, the intercalation of graphite, the commercialized anode material of LIBs, cannot be established effectively with sodium ions. Also, the electrode materials for SIBs still show poorer performances than LIBs, where their specific capacities (around 300–500 mAh g^{-1}) are far from satisfactory. Thus, it is a big mission for researchers to find suitable electrode materials to increase the binding energy and subsequent capacities to improve the performance of SIBs.

Na metal is regarded as the ideal anode for SIBs. However, the Fermi energy (E_F) of the most non-aqueous electrolytes crosses the LUMO. By forming a passivation layer of the SEI (solid electrolyte interphase), the Na in the half-cell can introduce the electrochemical behavior of electrode materials. However, this layer (SEI) is risky to break up due to the formation of the dendrites under continuous charging and discharging cycles, and thus a short circuit of the battery will happen [81]. With better electrode materials, SIBs follow criteria similar to LIBs like higher power density, energy density, environmental friendliness, safety, more shelf time, and low-cost [82,83]. The cost of a battery is related to the electrode materials used and shelf lifetime. During the usage of a cell, safety depends on the stability of electrodes and electrolytes [84,85]. In terms of voltage and capacity, the cell energy density is defined by,

$$E = \int_0^Q QV(q)dq \tag{4}$$

In the above equation, $V(q)$ corresponds to the voltage at the charge state q and Q is the specific capacity of a cell. The voltage is caused by the difference between the anode and cathode potentials.

If the capacity and the voltage are higher, the energy density will be higher. To operate efficiently, a high-voltage cell must have a cathode with a higher potential and an anode with a lower potential. The power density ($P(q) = V(q)I_{dis}$) depends on the discharge current and voltage of the cell. The voltage ($V(q)$) has a dependency on the charge state (q) and

the discharge current (I_{dis}) because of different over-potentials (η) at different currents. The over-potential reduces the discharge voltage ($V_{dis} = V_{oc} - \eta$ (q, I_{dis})) and increases the charge voltage ($V_{ch} = V_{oc} + \eta$ (q, I_{ch})). Thus, a low over-potential is needed to obtain high power density. To attain a low over-potential, a cell requires high electronic conductivity, fast reaction kinetics, and low activation barrier for Na ion migration in electrodes and electrolytes.

Pre-sodiumization technology can effectively supplement the irreversible sodium loss during cycling, so it plays a crucial role in the practical application of SIBs. The common pre-sodiumization methods include electrochemical pre-sodiumation, chemical pre-sodiumation, physical pre-sodiumization, and cathode additives. Electrochemical and chemical pre-sodiumization can obtain a stable solid electrolyte interphase (SEI) film but is limited by complicated processes and the high cost. The positive electrode additive is simple and convenient to operate, but it is unavoidable to introduce some residue. Physical pre-sodiumization is easy to operate, but safety is a challenging problem. Researchers designed the molten sodium method to reduce the growth of Na dendrite and the potential safety issue of physical pre-sodiumization.

Low-dimensional nanomaterials were recently explored for SIBs owing to their large surface area and outstanding electronic properties [87–91]. Graphene was first explored because of its rich abundance, thermal stability, and high carrier mobility [92,93]. However, a perfect graphene monolayer hardly adsorbs Li atoms [94]. Consequently, various modified graphene, including defective graphene [95,96], doped graphene [97], graphene nanoribbon [98], and some other low dimensional materials including graphene [99], phosphorene [100–102], and MXenes [90] have been explored for SIBs. These studies demonstrated that the dimension and morphology of the edge influence the energy density of anode materials remarkably.

3. Computational methods to study electrode materials for SIBs

3.1. Structural stability calculations

The stability of an electrode material can be investigated theoretically by computing formation energy (E_f). Using SnC as an example, the formation energy of SnC can be calculated by the equation, $E_f = -(E_{Sn} + E_C) + E_{SnC}$; where, E_{Sn}, E_C, and E_{SnC} are the energies of bulk Sn, bulk C, and monolayer SnC. If the E_f value is more negative, the structure is more likely to be synthesized.

The thermodynamical stability of an electrode material can be analyzed by performing the first-principles Ab-initio molecular dynamic (AIMD) simulations. Molecular dynamics (MD) refer to analyzing the physical motions of atoms and molecules under certain conditions of temperature and pressure. The interactions of atoms and molecules are enabled at a fixed time, thus revealing the system dynamics. The most customary version of molecular dynamics predicts atoms' and molecules' trajectories by solving Newton's equations of motion numerically for interacting particles system. Interatomic potentials or molecular mechanics force fields are commonly utilized to compute the forces between particles and their potential energies. Among the main applications are chemical physics, materials science, and biophysics. The properties of molecular systems cannot be analytically established as they are regularly composed of many particles; numerical methods are applied to overcome this dilemma in MD simulation. The initial structure after geometrical optimization is used to perform the thermal processes at different temperatures such as T = 300 K, 500 K, or 1000 K for five ps and ten ps. After that, one can easily find the energy fluctuations (eV) versus time duration (fs) plot and explore the geometries during and after AIMD simulations, thus evaluating the thermal stability of electrode materials at different temperatures.

Next, the dynamical stability can be analyzed by phonon dispersion calculations. In addition to exchanging the kinetic and potential energies, the crystal lattice is constantly oscillating around its equilibrium

position. The zero-point energy describes the vibrational energy associated with these oscillations that continue at 0 K. When the temperature is raised, the lattice vibrations become more pronounced in amplitude. Hence, a phase transition is evident as the temperature rises. Ideally, the atoms should act as a bound system at a certain temperature (~0 K at least) to acquire the material's dynamical stability, which can be explained by its phonon dispersion. Since graphene is the basis for 2D materials, we choose penta-graphene to present computational results and analysis of its structural stability. As shown in graph 2, the phonon band structure spectrum, structural geometry, and phonon DOS of dynamically stable penta-graphene are described. The material is dynamically unstable when a phonon branch softens in the Brillouin zone. In other words, the square of the frequency evaluated from the dynamical matrix has a negative value that produces an imaginary frequency. This mode does not produce sufficient restoring force to cause lattice vibrations, signifying that the material experiences a transition state. There are three types of acoustic modes in a phonon dispersion spectrum of a material, namely (i) the flexural acoustic (ZA) mode, (ii) the transverse acoustic (TA) mode, and (iii) the longitudinal acoustic mode (LA), correspondingly. While all three branches are linear as q → 0 in bulk materials, the ZA branch displays quadratic behavior in their monolayers [103]. Comparative to the other branches, the ZA branch exhibits a softening nature in the phonon dispersion of monolayers. Some monolayers exhibit soft ZA branches at q → 0 that correspond to their instability. It is possible to eliminate such instability by inserting defects [104]. Usually, soft modes in the phonon dispersion of material are signs of its dynamical instability, but this may not apply in all cases. Occasionally, the ZA mode softness at a point far from the Γ-point is caused by an instability in the charge density wave, which can be eliminated through the increment in the electronic smearing [105]. Togo et al. developed a phony code that is useful for researchers to analyze the material properties associated with the lattice dynamics [106].

To maintain its unstrained structure, a new theoretically designed electrode material composed of a suspended monolayer structure must meet mechanical stability criteria. The criterion of born stability for crystalline structures with high symmetry was first published in 1954 and applied widely by various researchers since then. Nevertheless, this criterion is insufficient for treating complex symmetries in critical conditions. It was later extended to other structure types as well. Considering a crystalline lattice with equilibrium volume V_0 and energy E, the second-order elastic constants are defined as $C_{ij} = \partial^2 E /(V_0 \partial \varepsilon_i \partial \varepsilon_j)$, where the strain is designed by ε_{bj}. There are 15 dependent and 21 independent elements in the 6×6 supercell. When a homogeneous infinitesimal strain is applied to a crystal through a virtual displacement, its energy will vary by $E = E_0 + \frac{V_0}{2}\sum_{i,j=1}^{6} C_{ij}\, \varepsilon_i\, \varepsilon_j + O(\varepsilon^3)$. All $\varepsilon \neq 0$ and $E > 0$ will result in mechanical stability. For crystal structure stability, Born established four essential and enough factors without considering crystal symmetry. According to ref [107], the Born stability criteria can be used to determine necessary but insufficient conditions in terms of elastic coefficients:

$$C_{ii} > 0, C_{ij}^2 < C_{ii}C_{jj}, \forall_{i,j}$$

The required and optimal stability conditions for certain crystal systems, such as cubic systems, are described in Ref. [107]:

$$C_{11} - C_{12} > 0, C_{11} + 2C_{12} > 0, C_{44} > 0$$

Hexagonal and tetragonal systems:

$$C_{11} > C_{12}, 2C_{13}^2 < C_{33}(C_{11} + C_{12}), C_{44} > 0, 2C_{16}^2 < C_{66}(C_{11} - C_{12})$$

Orthorhombic systems:

$$C_{ii} > 0, C_{ii} + C_{jj} - 2C_{ij} > 0, C_{11} + C_{22} + C_{33} + 2(C_{12} + C_{13} + C_{23}) \rangle 0$$

Rhombohedral systems:

$$C_{11} > |C_{12}|, C_{44} > 0, C_{13}^2 < \frac{1}{2}C_{33}(C_{11} + C_{12})C_{12}^2 + C_{15}^2 < \frac{1}{2}C_{44}(C_{11} + C_{12}$$
$$\equiv C_{44}C_{66}$$

In density functional theory, the lattice is applied in computational modeling, and the three-dimensional periodic boundary conditions are also involved. It is necessary to renormalize the elastic constants (C_{ij}^{2D}) concerning the distance c between the periodic layers [108], in such a way $C_{ij}^{2D} = cC_{ij}^{3D}$. For 2D materials, some of the C_{ij} are worthless, making the Born stability criteria more straightforward. More precisely, mechanical stability can be analyzed by finding elastic constants and elastic moduli.

3.2. Estimation of the binding energy of Na on electrode material for SIBs

For an efficient Na anode material, the adsorption of Na ions is achieved with high binding strength. To calculate the binding energy, we should consider different Na loading sites on the structural surface. The binding energy (E_b) of Na adsorption on A (anode material) can be calculated using the formula [109],

$$Eb = (E_{NaA} - E_A + nE_{Na})/n, \tag{5}$$

where E_{NaA}, E_A, and E_{Na} designate the energies of material A having Na adsorption, bare A, and metallic bulk Na, respectively. The term n used in the formula denotes the adsorbed Na atoms on A. The negative value of E_b means a favorable interaction between Na and A under an electrochemical state.

As representative examples, we considered the MoS$_2$, WS$_2$, MoSe$_2$, and WSe$_2$ monolayers, MoS$_2$/WS$_2$, and MoS$_2$/MoSe$_2$ heterostructures, which were proposed as anode materials for LIBs by Wang and co-workers. T and H sites were identified as potential adsorption sites in MoS$_2$, WS$_2$, MoSe$_2$, and WSe$_2$ monolayers (Fig. 2c). Also, their adsorption energies were computed using the energy of the Li bulk structure [39]. Adsorption energies at the T site are −1.85 eV (MoS$_2$), −1.46 eV (WS$_2$), −1.56 eV (MoSe$_2$), and −1.23 eV (WSe$_2$), whereas, those at the H site are −1.712 eV (MoS$_2$), −1.29 eV (WS$_2$), −1.39 eV (MoSe$_2$), and −1.112 eV (WSe$_2$) by using PBE functional. The negative adsorption energies purport that the Li adsorptions on these materials are exothermic and spontaneous. Moreover, the T site is more suitable than the H site, therefore, the path followed by Li is from the T site to the H site. Similarly, the lithiation/delithiation processes of heterostructure (MoS$_2$/WS$_2$) are examined. The activation barriers with their corresponding pathways are shown in Fig. 2d. The two pathways are H-T$_{Mo}$-H and H-T$_w$-H with their corresponding energy barriers of 0.22 eV and 0.30 eV, individually.

The single-atom adsorption strength gives us the fundamental possibility of using a material as an electrode, while more atoms adsorption on the surface would be relayed for the storage capacity, which directly affects the performance of a battery.

3.3. Theoretical storage capacity of electrode material for SIBs

Electrode material possesses a specific storage capacity in proportion to the amount of adsorption of Li/Na. After a single Li/Na atom is adsorbed, we can investigate adsorption behavior that is concentration-dependent on Li/Na atoms. Negative adsorption energy should confirm the relative stability of maximum coverage. Through the stable maximum coverage, we can obtain the coordinate chemical stoichiometry and calculate the theoretical storage capacity by the following equation:

$$Q_{theoretical} = (nF)/(M_w) \tag{6}$$

where $Q_{theoretical}$ is the theoretical specific capacity, the charge carrier number is defined by n, the Faraday constant (~26801 mAh mol^{-1}) is labeled by F, and M_w represents the molecular weight of the active
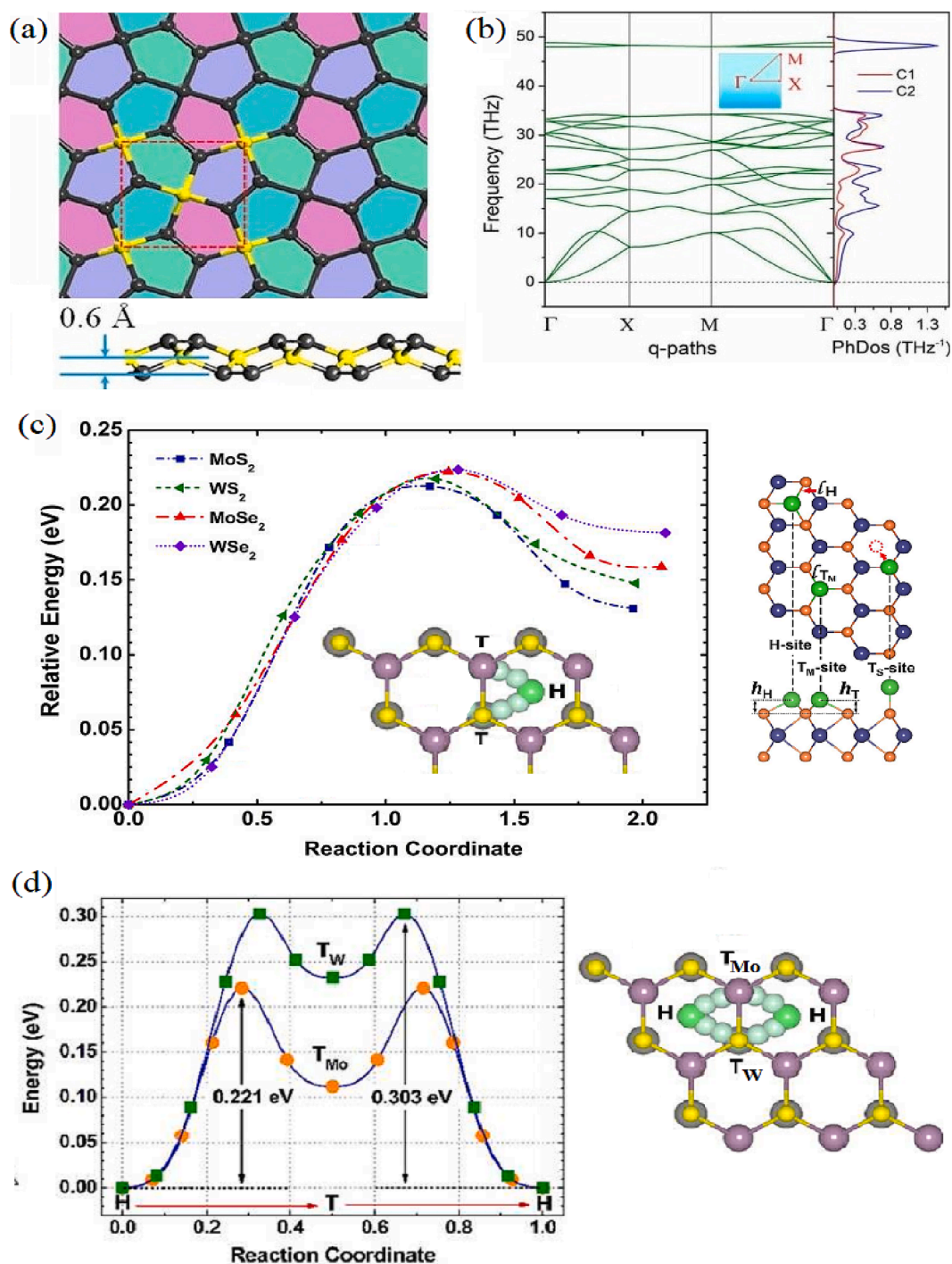
Fig. 2. The upper and lower plots in (a) depict the atomic structure of the penta-graphene in the top (upper panel) and side views (bottom panel) of the crystalline structure of the penta-graphene. The atomic structure displayed by the yellow and black colored spheres is associated with sp³ and sp² carbon atoms, correspondingly. (b) The phonon spectrum and phonon DOS of penta-graphene are displayed in the left and right sections, respectively. Reproduced from reference [110]. (c) Energy barriers for Li atom diffusion along the T to H site on monolayer MX₂ (M = Mo, W; X = S, Se), and top (above) and side (bottom) outlooks of three representative sites (H, T_{Mo}, and T_S) for Li adsorbed on monolayers MX₂. (d) The pathway and energy barriers for Li atoms diffused among two neighboring H sites bypass the T_W and T_{Mo} sites, respectively. Reprinted from Ref. [111].

materials. For example, a monolayer of TiC_3 is adsorbed by two layers of Na atoms on both sides, giving a TiC_3Na_4 monolayer, resulting in the highest adsorption of Na in TiC_3Na_4. Thus, the theoretical capacity of TiC_3 achieves 1278 mAh g⁻¹ [112], significantly higher than prior works on SIBs capacity (approximately 300–500 mAh g⁻¹). Using 2D materials as electrode materials for SIBs is made viable by the large capacity of TiC_3. The proposed reasons for the ultrahigh capacity are 1)

its *n*-biphenyl units on TiC_3 serve both as a high adsorption area, and significant adsorption energy for the Na atom; 2) its dispersive electron cloud functions as an anion, controlling the stabilization of Na adsorptions and favoring the multilayer adsorption. These computational simulations identified constraining parameters for batteries and helped clarify the underlying mechanism of the performance. To further clarify the theoretical storage capacity, let us take an example of monolayer

SnS_2. As shown in Fig. 5c, Na content is adsorbed on a $3 \times 3 \times 1$ SnS_2 supercell with all top and bottom H-sites occupied by Na. Since a $3 \times 3 \times 1$ SnS_2 supercell has 9 atoms of Sn, so a total of 18 atoms are adsorbed on the SnS_2 supercell. Therefore, the calculated theoretical capacity of Na_2SnS_2 is ($Q_{theoretical} = (nF/M_w = 2 \times 26801/182.81) \sim 293$ mAh g^{-1}.

3.4. Computations of open-circuit voltage of electrode material for SIBs

The performance of an anode is checked by an essential parameter known as open-circuit voltage (OCV). Metal-ion batteries need a high half-cell voltage from the cathode and a low half-cell voltage from the anode to achieve a net high cell voltage [113,114]. In the case of SIBs, the reaction of the typical half-cell during the charging/discharging procedure at the anode (A) is defined by the relation, $A + xNa^+ + xe^- \leftrightarrow Na_xA$ [115]. The positive ions move between electrolyte and electrodes during this reaction while electrons flow across the outer battery circuit. When neglecting the pressure, temperature, and entropy impacts, the OCV for Na adsorbed A is given by the formula,

$$[OCV = E_{Na_{x1}} - E_{Na_{x2}} + (x_2 - x_1) E_{Na} / (x_2 - x_1)e \tag{7}$$

where the energy of $Na_{x1}A$ is defined by $E_{Na_{x1}}$, the energy of $Na_{x2}A$ is represented by $E_{Na_{x2}}$, and E_{Na} describes the bulk Na energy determined from first-principle calculations at 0 K. Low OCV of the anode material correspond to the btter performance of the batteries. For SIBs applications, the computed average voltage profile of a prospective anode material should be lower or in the range of commercialized anode materials (i.e., 0.11 V for graphite and 1.5–1.8 V for TiO_2) [116–118].

The equilibrium voltage of Mi intercalation is calculated by the difference in chemical potential of Li/Na/K ($\mu_{Li}/\mu_{Na}/\mu_K = \mu_{Mi}$) between anode and cathode, i.e.

$$V = (-\mu_{Mi}^{cathode} - \mu_{Mi}^{anode})/zF \tag{8}$$

where F is the Faraday constant (26801 mAh mol^{-1}), Mi denotes metal ions, and z is the charge transferred. With Li/Na/K content, the μ_{Mi} is the change of the free energy of the electrode material. By integrating the above equation over a finite amount of reaction, one can obtain the average voltage as a function of the free energy change of the combined anode/cathode reaction (Nernst equation).

$$V = \Delta G_r/zF \tag{9}$$

The entropic contributions to ΔG_r are negligible at low temperatures, and the reaction-free energy is approximately equal to the internal energy ($\Delta G_r \approx \Delta E_r$). Within this approximation, we consider the equilibrium voltage of a lithium transition-metal oxide intercalation cathode with composition $MiMO_2$ and a lithium metal ion anode as an example. The cell reaction is given by,

$$Mi_{x1} MO_2 \longrightarrow Mi_{x2} MO_2 + (x_1 - x_2)Mi \tag{10}$$

$$[V(x1, x2) = E_{Mi_{x1}}MO_2 - E_{Mi_{x2}}MO_2 + (x_2 - x_1) E_{Mi}]/(x_2 - x_1)e \tag{11}$$

where the energies of the $E(Mi_{x1} MO_2)$ and $E(Mi_{x2}MO_2)$, and bulk Li/Na/K (E_{Mi}) can be predicted from first principles investigations.

3.5. Diffusion mechanism in SIBs

Electrode materials should possess prompt electrons and ion transportation for degrading the battery's sodiation and desodiation duration. Na diffusion with fast kinetics is directly linked to the rate capability. Therefore, the energy surface of an anode material with Na is better in-sighted using nudged elastic band (NEB) method [119,120]. Based on DFT calculations, minimum energy paths (MEPs) can be computed to find the activation barriers and the difference between the lowest and highest point energies on the MEP. The diffusion barrier is directly linked to the sodiation and desodiation processes in SIBs. The lower the activation barrier, the faster the charging and discharging

processes will be. There is also another method known as the climbing-image NEB (CI-NBE) technique used to obtain more accurate estimated results of energy barriers. In the NEB method, a climbing image is introduced (LCLIMB =.TRUE. in Vienna Ab initio Simulation Package), which drives the highest energy image to the saddle point [121]. However, NEB calculations are somehow complicated in many SIBs electrode materials such as layered metal oxides Na_xMO_2 have complicated Na orderings at different Na content [122]. This may lead to a complex diffusion process. For all possible diffusion of Na, it is arduous to estimate which diffusion mode is leading and whether diffusion would happen or not.

In exploring TiC_3 in SIBs, diffusion pathways are plausible for the sodium atoms in sites A_1 and A_2 (Fig. 4c, d, the path I and II) by the NEB method [40]. The induced diffusion energy barrier equals 0.18 eV for the path I ($A_1 \rightarrow A_2 \rightarrow A_1$). However, in the case of path II, the motion of Na ion takes place unequivocally through the A_1 site to the adjacent A_1 site, and its diffusion energy barrier is 0.31 eV. The lesser energy barrier yields quicker transportation, so Path I will be preferable. Moreover, a lesser diffusion energy barrier is achieved for Path I because of the aromatic C_6 rings.

NEB calculations combined with MD simulations explore the complex diffusion processes and are supportive of investigating diffusion mechanisms [123,124]. Ab initio MD (AIMD) simulations have great success in explaining and identifying the diffusion mechanisms with more reliable diffusion barriers results based on DFT [125,126]. However, AIMD simulations need a higher computational cost for a few hundred atoms at elevated temperatures (>600 K). Similar to experimental results, AIMD computations define the ion conductivities and diffusivities at various temperatures. The diffusivity at a temperature T can be calculated by following the Arrhenius relation,

$$D(T) = D_0 \, e_B^{TEa/k} \text{ (viii)}.$$ where D_0 is the diffusivity at a temperature T_o, e is the charge of Na ion, E_a is the activation energy (diffusion barrier), k_B designates the Boltzmann constant (1.38×10^{-23} J K^{-1}), and T represents the temperature. One can easily find the activation energy barrier by rearranging the Arrhenius equation. The diffusion barrier of phosphorene for magnesium ion batteries is calculated by using this equation [127].

4. 2D metal sulfides and carbides

The family of 2D materials has grown from graphene to metal sulfides, carbides, nitrides, oxides, etc., and are excellent host materials for energy storage applications. 2D structures may have high ion adsorption capability and faster ion transport between the layers. Fig. 3 depicts some well-recognized layered 2D materials that can be employed as anodes for rechargeable batteries.

Among 2D materials, carbon-based layered MCs, such as Mo_2C, Sc_2C, V_2C, TiC, W_2C, NiC_3, and PC_3 are promising host materials for Na intercalation due to the more considerable interlayer distance than Na$^+$ size. The natural abundance of carbon-based materials makes them attractive host materials for energy storage devices. LIBs use graphite as their most active anode material. In the case of SIBs, graphite has a low Na$^+$ storage capacity due to the larger size of the Na ion than the lithium-ion.

Metal sulfides (MSs) are also commonly applied in energy storage devices, including supercapacitors, fuel cells, LIBs, and SIBs [128–132]. Moreover, the weaker bond in M−S corresponds to much better electrochemical activity for reversible Na ion storage. The layered structures of MSs (M = Mo, Sn, W, V, etc.) are similar to graphite showing excellent cycling performance [133–138]. Furthermore, the better rate capability of MSs in SIBs is another critical parameter when selecting future anodes.
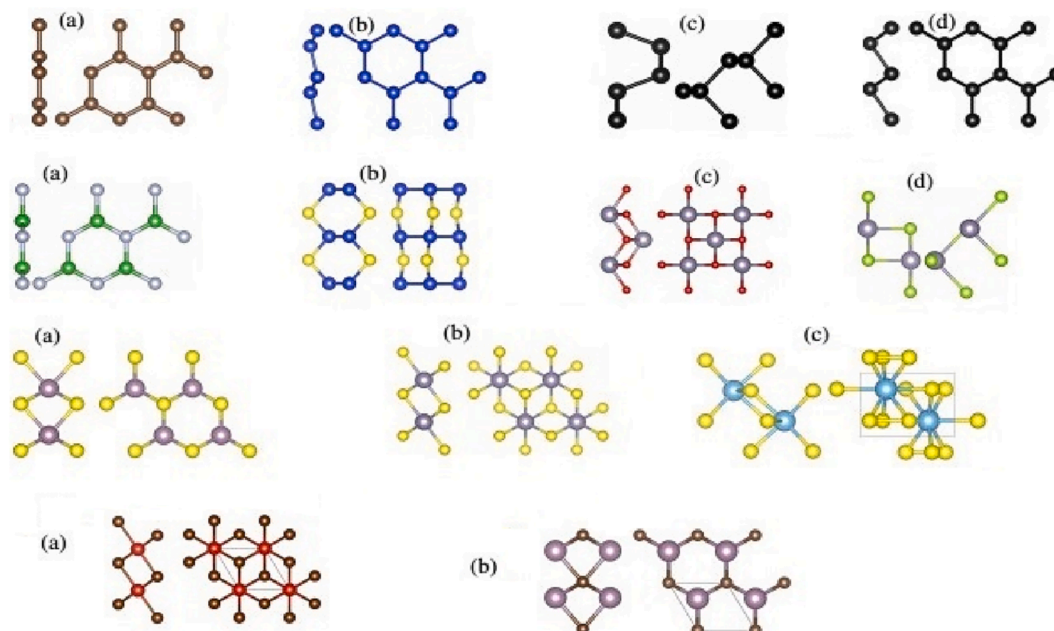
Fig. 3. Prototype structures for 2D materials. Row 1 shows top and side snapshots for (a) graphene, (b) silicene, (c) black phosphorene, (d) blue phosphorene. Row 2 shows side and front outlooks of monolayer (a) *h*-BN, (b) SiS, (c) SnO, (d) SnSe. Row 3 shows front and side outlooks of 2D (a) 2H MoS$_2$, (b) 1 T SnS$_2$, and (c) TiS$_3$. Row 4 shows side and top outlooks of single layer (a) VBr$_2$ and (b) Mo$_2$C. Reprinted from Ref. SPS:refid::bib139[139].

4.1. Metal sulfides

4.1.1. Vanadium sulfide (VS$_2$)

The structure of VS$_2$ is composed of V and S atoms, where the V atoms layer is placed between two S atoms layers. 2D VS$_2$ crystalizes in two polymorphs such as hexagonal (H) and trigonal (T). In these two polymorphs, H-phase is more stable than *T*-phase at room temperature. Therefore, H-phase is considered for battery applications using DFT investigations. Here, a = b = 3.17 Å represents the theoretically optimized lattice constants, and the bond lengths of V-S and S—S are 2.34 Å and 2.97 Å, respectively. Theoretical calculations reveal that bare VS$_2$ is metallic [140]. For Na storage, the VS$_2$ monolayer was investigated by Putungan et al. using DFT calculations. The charging/discharging processes of both phases, i.e., the computed energy barriers for Na migration, are ~ 0.085 eV and 0.088 eV for H and T, respectively as shown in Fig. 3c, d. For Na adsorbed H and T phases, the average OCV is estimated at 1.30 V and 1.42 V, respectively. Furthermore, the calculated capacity of the H and T phases are 232.91 mA g h^{-1} and 116.24 mA g h^{-1}, respectively [141].

Experimentally, Feng et al. employed a distinctive ammonia-supported procedure to exfoliate bulk flakes of VS$_2$ into ultrathin nanosheets of VS$_2$ stacked with fewer than five S–V–S monolayers, establishing a new type of 2D material with metallic characteristics independent of graphene [142]. In another study, highly layered crystalline VS$_2$ nanosheets of 50 nm thickness were fabricated via a solvothermal technique, and their electrochemical outcomes were investigated. Following 30 cycles, a remarkably large reversible capacity of 532.2 mAh g^{-1} was detected for VS$_2$ nanosheets at 50 mA g^{-1}. Furthermore, after 100 cycles, stability in discharge capacities is preserved at 436.8 and 270.4 mAh g^{-1} at 100 and 500 mA g^{-1}, correspondingly. Owing to the well-established layered structure and greater electronic conductivity, the device is attributable to long-lasting cycling stability and high-rate capability [143]. In a simple one-step polyvinylpyrrolidone (PVP) supported assembly technique, Sun and his co-workers fabricated a newly layer-by-layer VS$_2$-stacked nanosheet (VS$_2$-SNSs). For SIBs applications, VS$_2$ offers outstanding electrochemical performance because of its highly stable and ordered stacking-layer structure. When functioning at 0.2 A g^{-1}, it is feasible to acquire a reversible discharge capacity of 250 mAh g^{-1}. A maximal specific capacity of 150 mAh g^{-1} is achieved (discharge/charge rate of 27 s), even when operating at 20 Ag^{-1}. An additional benefit of the VS$_2$-SNSs is connected to lengthy deliver cycling duration, without capacity degradation by operating at 5 A g^{-1} even after 600 cycles. Ex-situ TEM and in-situ XRD analysis indicate that VS$_2$ undergoes a reversible intercalation reaction behavior. A systematic electrochemical kinetic inspection indicated that the intercalation pseudocapacitive mechanism is with up to 69 % capacitive contribution for the total capacity at one mV s^{-1}. Given its remarkable electrochemical performance, the VS$_2$ stands out as an ideal applicant for the next generation of large-scale energy storage devices [144].

Few-layer nanosheets are therefore an alternative way to enhance the working of batteries. A simple solvothermal method was used to produce VS$_2$ with a thickness of around 9 nm. Fig. 4a illustrates the assemblies of VS$_2$ nanosheet in the range of 500 nm^{-1} μm with approximately 10 atomic layers. These sheets thus give short diffusion paths for sodium ions and display an exceptional performance; even at less than 1 and 2 A g^{-1}, they still exhibit capacities of 550 and 400 mAh g^{-1}, respectively, as shown in Fig. 4b [145].

4.1.2. Titanium sulfide (TiS$_2$)

2D TiS$_2$ consists of two polymorphs (2H or 1 T) under normal temperature and pressure conditions. After relaxing the two structures, the most stable one is 1 T (due to higher binding energy) with lattice parameters a = b = 3.40 Å as well as bond length ~ 2.43 Å for Ti-S. Samad et al. studied the 1 T phase of TiS$_2$ for SIBs as anode material. Bare 1 T TiS$_2$ has a metallic character. Its electronic conductivity was improved after the adsorption of Na content. The low diffusion barrier (0.13 eV) governs fast charge/discharge processes. Its voltage profile is low, with a theoretical capacity of 478 mAh g^{-1}, beneficial for the SIBs [146]. Based on an experimental shear-mixing technique, Hu et al. successfully synthesized ultrathin TiS$_2$ nanosheets, which illustrated excellent cycling performance (386 mAh g^{-1} after 200 cycles when operated at 0.2 A g^{-1}. It is anticipated that this facile preparation technique will offer significant insights into the synthesis of ultrathin 2D materials with unique morphologies, which could greatly facilitate their use in rechargeable batteries [147]. Through another attempt, Chaturvedi reported 2D TiS$_2$
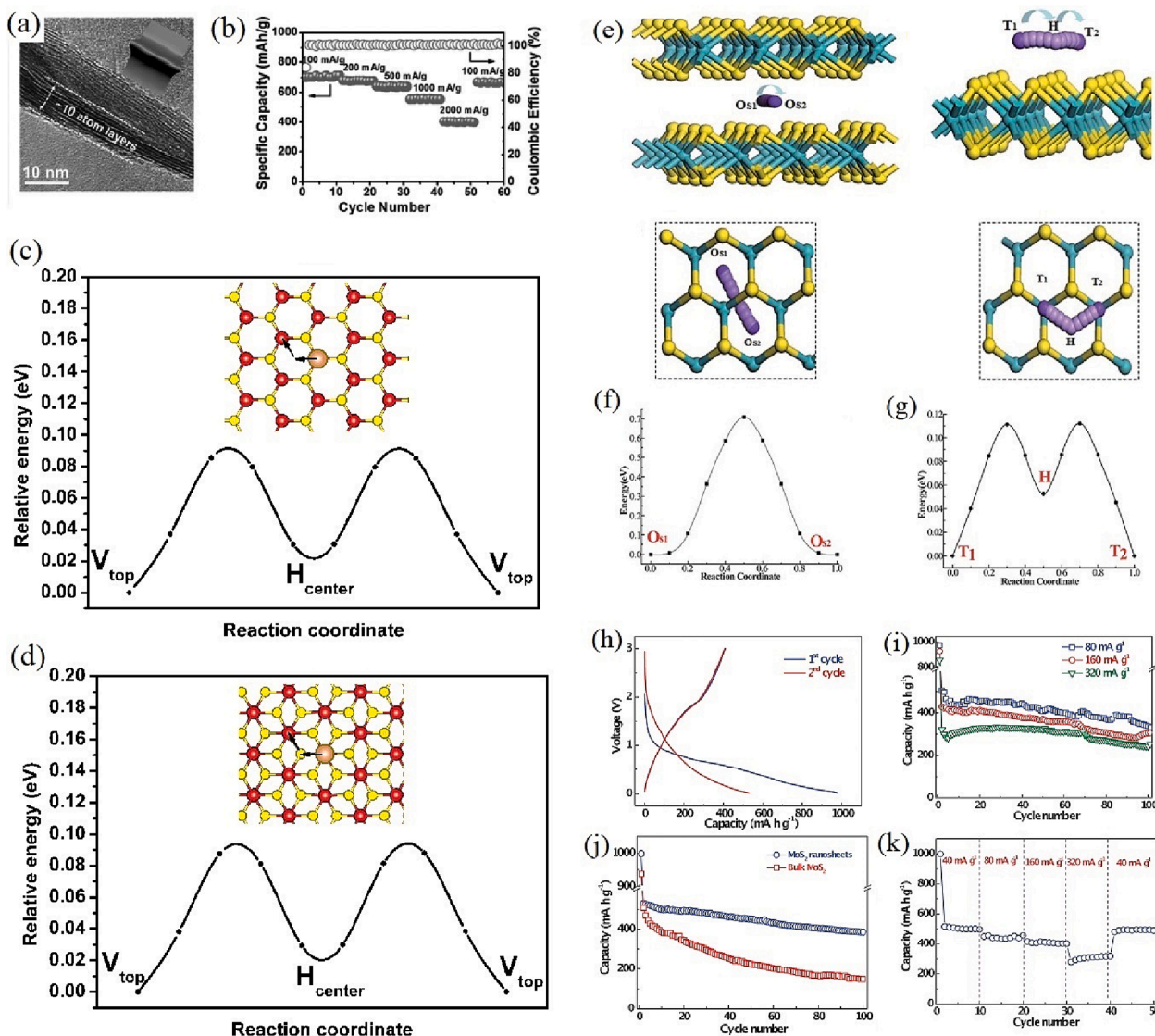
Fig. 4. (a) TEM image of VS$_2$ nanosheet assemblies. (b) Rate performance of VS$_2$ NSCS. Reprinted from Ref. [145]. (c) Reprinted from Ref. [141]. (e) Diffusion pathways with activation barriers for (f) bulk and (g) monolayer MoS$_2$. Reprinted from Ref. [151]. (h) 1st and 2nd cycle discharge and charge profiles of MoS$_2$ nanosheets at 40 mA g^{-1} current density. (i) Cycling performance of exfoliated MoS$_2$ nanosheets at current densities of 80, 160, and 320 mA g^{-1}. (j) Comparison of cycling performances of bulk and exfoliated MoS$_2$ nanosheet electrodes at 40 mA g^{-1} current density. (k) Rate performance of exfoliated MoS$_2$ nanosheets at varied current densities. Reprinted from Ref. [150].

by chemical vapor transport for SIBs. A reversible capacity of 146 mAh g^{-1} was found for the Na/TiS$_2$ cell when functioning at a 0.1C rate. TiS$_2$ offers outstanding cycling stability and rate performance. Cyclic voltammetry and impedance measurements can evaluate the charge storage process and interfacial characteristics. To establish the structural stability of the incorporation host, operand probing is also carried out [148].

4.1.3. Molybdenum sulfide (MoS$_2$)

Computationally, monolayer MoS$_2$ was characterized in 1 T, and 2H phases by Mortazavi et al. For both phases, the optimization of lattice parameters provides $a = b = 6.39$ Å (2H) as well as $a = b = 6.46$ Å (1 T). The electronic nature of both phases is semiconducting, and their corresponding bandgap values are 0.98 eV (1 T) and 0.90 eV (2H). As anode material for SIBs, the voltage profile spans between 0.75 and 1.25 V, while their capacity is 146 mAh g^{-1}. The diffusion barriers for both 1 T and 2H structures are equal to 0.28 eV and 0.68 eV, respectively, disclosing a fast charge/discharge process with better performance for the 1 T phase [115]. In another report on the first-principles analysis, Su

et al. discussed graphene-like MoS$_2$ monolayer with lattice constants of $a = b = 3.18$ Å and bond length of 2.41 (d_{M-S}) after optimization, which is useful for SIBs. It revealed semiconducting nature without the adsorption of Na. After the doping of Na content, the monolayer MoS$_2$ is metallic with high conductivity. It revealed a low voltage of 1.0 V upon sodiation, having a maximum capacity of 335 mAh g^{-1}. For the charge/discharge process, the activation pathways and the corresponding barriers for bulk (0.70 eV) and monolayer (0.11 eV) are shown in Fig. 4. These outcomes illustrated that monolayer MoS$_2$ is a prospective anode material for SIBs [149].

Su and his collaborators effectively prepared few-layered MoS$_2$ nanosheets through an ultrasonic exfoliation method that is scalable and straightforward MoS$_2$ nanosheets possess a thickness of approximately 10 nm, as determined via atomic force microscopy (AFM) and scanning electron microscopy (SEM). The exceptional nanosheet architecture of the MoS$_2$ crystalline structure is represented by its sizeable interlayer spacing (d (0 0 2) = 6.38 Å) and ultrathin thickness that results in the fast transport of sodium ions provided via the short diffusion paths. Fig. 4 depicts 1st and 2nd cycle discharge and charge curves of MoS$_2$
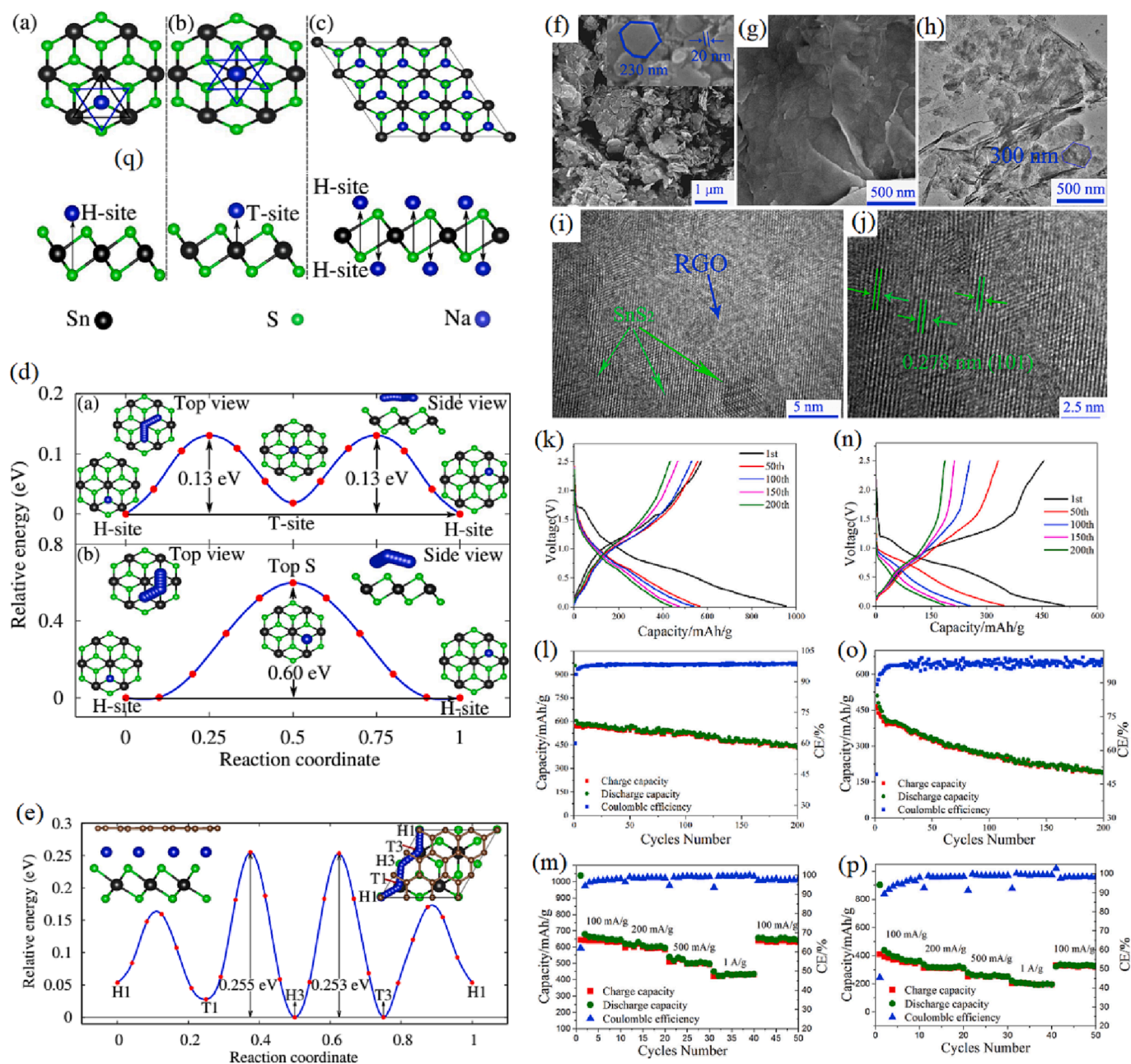
Fig. 5. (a) Descriptive spheres for Sn, Na, and S and the top and side outlooks of a portion of NaSnS$_2$ monolayer at H-site (b) Na at *T*-site (c) a 3 × 3 × 1 SnS$_2$ supercell with all top and bottom H-sites occupied by Na. (d) MEP for the Na diffusion for H-*T*-H site with an energy barrier of 0.13 eV. The trajectory of Na along the H-*T*-H path is given inset. (e) MEP for the Na diffusion for the H—S—H site with an energy barrier of 0.60 eV. The inset displays the trajectory of Na diffusion along the H—S—H path [155]. (f) SEM image of SnS$_2$, (g) SEM image, (h) TEM image, (i-j) HRTEM images of SnS$_2$-rGO composite material, (k) Charge/discharge curves, (l) cycling performance at a current rate of 100 mA g^{-1} over 200 cycles, (m) the rate performance of the SnS$_2$-rGO electrodes, (n) Charge/discharge profiles, (o) cycling performance at 100 mA g^{-1} over 200 cycles, and (p) the rate performance of the SnS$_2$ electrodes. Reproduced from Ref. [161].

nanosheets at 40 mA g^{-1} current density, cycling performance at current densities of 80, 160, and 320 mA g^{-1}, comparison of cycling performances of bulk and MoS$_2$ monolayer electrodes at 40 mA g^{-1} current density, and rate performance of exfoliated MoS$_2$ nanosheets at varied current densities. The optimal reversible Na storage capacity and outstanding cycle ability of MoS$_2$ nanosheets could offer potential applications as anode materials for SIBs [150]. Park et al. elaborated a scalable strategy for the preparation of few-layered MoS$_2$ composites integrated into hierarchical porous carbon (MHPC) nanosheets that will be utilized as anode materials for both LIBs and SIBs. The as-established MHPCs possess exceptional characteristics that could be useful as anode materials for LIBs and SIBs, while they exhibit prominent reversible

capacity and lengthy cycling performances, even at elevated current density. Accordingly, this material can transport reversible capacities of 732 and 280 mAh g^{-1} at 1 A g^{-1} after 300 cycles in LIBs and SIBs, correspondingly. These MHPC composites are extremely useful in various areas, based on these results [151].

4.1.4. Germanium sulfide (GeS$_2$)

Monolayer GeS$_2$ was proposed by Li et al. using computational calculations for batteries. The GeS$_2$ structure is depicted in Fig. 5a with front and side views. The relaxed lattice constants are represented by *a* = 4.45 Å and *b* = 3.46 Å. There are two different bond lengths (Ge-S), such as 2.42 Å (d_1) and 2.46 Å (d_2). GeS$_2$ is a semiconductor that may

hinder the potential usefulness of batteries. As anode material for SIBs, 2D GeS$_2$ owned a metallicity nature with a poor composition of adsorbed Na ions. Fig. 4b corresponds to a small average OCV of 0.23 V with an optimal capacity of 512 mAh g^{-1}. The charging/discharging process was predicted to be fast due to an insignificant diffusion barrier of 0.09 eV. The low activation barrier, high capacity, and conductivity of monolayer GeS$_2$ hold great potential for the SIBs [152].

Experimentally, ultrathin nanosheets composed of GeS$_2$ have a 1.1 nm thickness, as reported by Wang et al. As anodes for LIBs, the structure can efficaciously extend the electrode/electrolyte interface area, precipitating the ion transfer and buffering the volume dilatation. Taking advantage of these merits, the as-fabricated nanosheets of GeS$_2$ offer significant specific capacity (1335 mAh g^{-1} after performance of 0.15 A g^{-1}), exceptional rate performance (337 mAh g^{-1} after performance of 15 A g^{-1}), and stabilized cycling performance (974 mAh g^{-1} achieved at 0.5 A g^{-1} after 200 cycles). A significant characteristic of the synthesized Li-ion full cells is their robust specific capacity of 577 mAh g^{-1} after 50 cycles when working at 0.1 Ag^{-1}, as well as a maximal energy density of 361 W h kg^{-1} established at a power density of 346 W kg^{-1}. Given these findings, GeS$_2$ can be utilized as a high-performance anode material for LIBs [153,154] Using a topochemical conversion technique, Li and his coworkers developed a strategy for synthesizing the ultrathin GeS$_2$ nanosheets (1.2 nm thickness) as prospective anodes for Na storage. Using 2D ultrathin nanostructures mitigates the electrode–electrolyte contact obstacle encountered by bulk materials, resulting in shorter transfer/diffusion pathways for Na ions and electrons and outstanding rate performance. When operating at 10 A g^{-1} even after 2000 cycles, the ultrathin GeS$_2$ nanosheets can deliver an impressive capacity of 515 mAh g^{-1}. Moreover, an in situ/ex-situ probing illustrated that Na$^+$ intercalation/deintercalation into/from the interlayer zone of GeS$_2$ (GeS$_2 \leftrightarrow$ NaxGeS$_2$) is a successful procedure. As a result, the ultrathin GeS$_2$ nanosheets are an intriguing candidate for SIBs due to their stabilized high energy density (~213 W h kg^{-1}) of the sodium-ion full cell when combined with the modern Na$_3$V$_2$(PO$_4$)$_2$O$_2$F cathode [153].

4.1.5. Tin sulfide (SnS$_2$)

The structure of SnS$_2$ is energetically favorable in the 1 T phase with computationally optimized lattice parameters a = b = 3.69 Å and bond length (sn-S) of 2.596 Å. In recent years Samad et al. computed the electrochemical properties of pristine SnS$_2$ and SnS$_2$/graphene heterostructure as anode material for SIBs. The structural model is shown in Fig. 5a-c with front and side outlooks for Na adsorption on H-site, *T*-site, and top/bottom H-sites. According to their findings, bare SnS$_2$ has a low activation barrier, low half-cell voltage, and high Na storage capacity. However, the semiconducting nature and the large volume expansion caused due to Na loading hinder the potential usefulness of SnS$_2$ for SIBs. Therefore, SnS$_2$/graphene heterostructure was proposed to overcome the large volume expansion problem of low electronic conductivity and thus improve stability. The activation barriers of the SnS$_2$ nanosheet and SnS$_2$/graphene heterostructure are shown in Fig. 5d and e, respectively. It is noted that the graphene layer enhanced the electronic conductivity. Moreover, the diffusion barrier was even lower in SnS$_2$/graphene heterostructure than in bare SnS$_2$, rendering it a suitable anode material beneficial for SIBs [155].

In the experimental work, Thangavel and his collaborators utilized an easy procedure based on simple microwave irradiation to fabricate 2D SnS$_2$ composed of a few layers onto graphene sheets for several minutes. Sodium-ion storage kinetics are characterized by rapid, nondestructive pseudo-capacitance and many surface sites in SnS$_2$. It was recently revealed that Na-ion storage with a significant current density of ~ 12 A g^{-1} could be enhanced substantially with remarkable reversibility and strong stability. Further, a realistically crafted sodium ion full cell that is joined to SnS$_2$/Na$_3$V$_2$(PO$_4$)$_3$ was demonstrated with strong stability, high performance (its excellent original Coulombic efficiency ~ 99 %), marked capacity, as well as retaining 53 % of the

starting capacity after rising the current density by a factor of 140.

Furthermore, both anode and cathode mass result in great specific energy of 140 W h kg^{-1} and an exceedingly-high specific power of 8.3 kW kg^{-1}. The excellent performance and facile fabrication of the few-layered SnS$_2$ make it an impressive contender for the realistic implementation of high-power SIBs [156]. In another experimental report, Zhou originally described the architecture of SnS@graphene that holds promise for SIB anode composed of 2D SnS and graphene nanosheets as auxiliary building blocks. Upon 250 cycles at 810 and 7290 mA g^{-1} current density, the as-fabricated hybrid nanostructured SnS@graphene composite achieves a 940 mAh g^{-1} marked specific capacity and a maximal rate capability of 492 and 308 mAh g^{-1}, respectively. The performance was superior to the most common anode materials reported for Na-ion batteries. The design process of SnS@graphene and the synergistic Na-storage reactions of SnS in the anode is described exhaustively by utilizing a combination of ex-situ X-ray diffraction, X-ray photoelectron spectroscopy, and ex-situ Fourier transform infrared spectroscopy.

During the sodiation procedure, it was observed that the SnS$_2$ underwent a three-phase structural transformation (from hexagonal- SnS$_2$ into tetragonal-Sn into orthorhombic- Na$_{3.75}$Sn). In contrast, the SnS is subjected to a two-phase structural transformation (from orthorhombic-SnS into cubic-Sn into orthorhombic-Na$_{3.75}$Sn). Since SnS undergoes lower structural variations over the conversion, its sodium-ion battery performance is anticipated to be impressive concerning strong structural and high-cycling stability. Based on these determinations, the architecture of SnS@graphene exhibits exceptional features that make it an attractive candidate for high-performance energy storage usage [157].

2D SnS$_2$-rGO as the anode material in Na-ion batteries was synthesized and electrochemically characterized by Mao et al. The morphology and microstructure of SnS$_2$ and SnS$_2$-rGO were given by the SEM and TEM images. The irregular sheet structure of SnS$_2$ has a size between 200 and 500 nm and a thickness of approximately 20 nm, as seen in Fig. 5 (f). Moreover, SEM and TEM images of the SnS$_2$-rGO composite are given in Fig. 5 (g and h). A few lattice fringes in the HRTEM image of the SnS$_2$-rGO composite material displayed in Fig. 5 (i) are not fuzzy and continuous, which corresponds to the HRTEM image of rGO. The clear and continuous part had a lattice fringe spacing of 0.278 nm, as seen in Fig. 5 (j). This is closely matched with the d value of the hexagonal phase SnS$_2$ (101 faces). Thus, this demonstrates that the sample is an SnS$_2$-rGO composite material. Sodium storage performance tests were performed on the SnS$_2$ and SnS$_2$-rGO materials. The charge–discharge curve at a current density of 100 mA g^{-1} of the SnS$_2$-rGO material is shown in Fig. 5 (k). The curve has a different slope between the first circle and the next cycle, which can be attributed to the layer space of Na inserted in SnS$_2$ and the alloying reaction. This is in complete agreement with the CV curve. The cycling profile of the SnS$_2$-rGO composite at a current density of 100 mA g^{-1} is presented in Fig. 5 (l). The discharge capacity at the start reaches up to 956.1 mAh g^{-1}, and after 200 cycles it drops to 443.4 mAh g^{-1}, declining at a rate of less than 0.5 % per cycle. This signifies the exceptional cycle stability of SnS$_2$-rGO composite material. The performance of the cycling of pure rGO electrode was confirmed at a current density of 100 mA g^{-1} for the determination of the capacity participation of rGO to the electrode material. A solid electrolyte mesophase (SEI) layer was formed due to the low Coulomb efficiency of the first circle (60 %) that is due to the irreversible transformation reaction. Nevertheless, a much lower starting Coulombic efficiency is seen for the SnS$_2$ nanosheets from the second circle. Finally, the Coulomb efficiency is higher than 90 % and stabilizes at approximately 99 %. Fig. 5 (m) displays the rate performance trend of the SnS$_2$-rGO composite material. The SnS$_2$-rGO electrode keeps a mean discharge capacity of 660.6, 610, 500.5, and 433.0 mAh g^{-1}, under the testing condition of 100, 200, 500, and 1000 mA g^{-1}, separately. Furthermore, after the return to 100 mA g^{-1}, the SnS$_2$-rGO electrode material keeps a mean discharge-specific capacity of 577.1 mAh g^{-1}, which shows excellent performance. SnS$_2$ has a decreased battery capacity compared to SnS$_2$-rGO as indicated by

the electrochemical performance of SnS_2 material shown in Fig. 5 (*n*-p). The discharge capacity is 189.2 mAh g^{-1} after 200 cycles for the test condition of 100 mA g^{-1}. Also, the discharge capacity is 210 mAh g^{-1} after 200 cycles for the test condition of 1000 mA g^{-1}. In addition, the electrical conductivity is improved after the presence of rGO in the SnS_2-rGO electrode material. This helps in assisting with the pressure of the volume variation during the deintercalation and insertion of Na ions, as well as improving the electrochemical performance of SnS_2 materials [141].

4.1.6. Silicon sulfide (SiS)

Jiang et al. studied the Na storage mechanism in SiS monolayer with relaxed lattice constants, as indicated by a = 4.60 Å and b = 3.27 Å using DFT investigations. Electronic conductivity is a crucial parameter for battery applications. Pure SiS exhibits a semiconducting attribute, and its corresponding bandgap is about 1.40 eV. However, the conductivity of 2D SiS increases after adsorbing a small content of Na atoms, which is a positive sign for high-performance SIBs. The simulated results reveal that a large amount of Na content is adsorbed in SiS with a theoretical capacity of 445.6 mAh g^{-1}. Furthermore, Na diffusion in SiS was calculated by the NEB technique. Three different pathways were simulated (Fig. 5) and its estimated activation barrier was insignificant at ∼ 0.135 eV showing high charge/discharge processes [158]. Pham et al. reported 2D SiS as an anode material for SIBs via DFT studies in another effort. 2D SiS revealed metallic nature with the adsorption of Na content. A maximum Na storage capacity of 187.2 mAh g^{-1} was achieved. The simulated low diffusion barrier (183 MeV) for the corresponding path has confirmed that Na migration in SiS is fast with high charging and discharging rates. These fascinating characteristics make the SiS monolayer promising for Na storage [159].

4.1.7. Yttrium sulfide (YS₂)

YS_2 crystalizes in the trigonal *Pm1* phase, energetically more stable than other proposed structures. Therefore, the *Pm1* phase of YS_2 was investigated for the battery applications using DFT investigations. The lattice parameters were optimized, and their values are $a = b = 4.024$ Å, while the Y-S bond length is equal to 2.702 Å. The S-Y-S and Y-S-Y bond angles are 83.74° and 96.26°, respectively. Using DFT investigations, the stable structure of monolayer YS_2 was predicted for SIBs by Guo et al (this line can be removed). The 2D YS_2 was confirmed to be dynamically and thermally stable due to the simulations of phonon spectrum ab-initio molecular dynamics (AIMD). The electronic conductivity was maintained during the sodiation process. Besides this, the calculated activation barrier (0.24 eV) was comparatively low with a fast Na ion migration rate. A maximum capacity of 350 mAh g^{-1} was obtained, making it suitable as an anode material for SIBs [160].

2D YS_2 with numerous structures such as (i), (ii), (iii), (iv), (v), and (vi), and their associated space group (obtained by CALYPSO code). The S and Y atoms are designated by purple and brown balls, respectively [160]. Energy profiles of Na diffusion on (a) SiS. The diffusion pathways (top and side views) of Na along (b) path 1, (c) path 2, and (d) path 3, reproduced from Ref. [158].

4.1.8. Phosphorous sulfide (PS₂)

Employing first-principles calculations, a 1 *T*-type PS_2 monolayer was investigated by Zhou et al. The structure of PS_2 is one of the AB_2 structures, and the 1 T phase is more stable energetically than the 2H phase. It has a similar structure, 1 T-MoS_2 containing three sub-planes. Interposed between the two sub-planes of sulfur atoms is the sub-plane of P atoms. The optimization of P—S distance and the lattice constants are 2.334 Å and $a = b = 3.288$ Å, respectively. To scrutinize the behavior of the electronic features of PS_2, the electronic DOS and band structures were calculated. The results revealed a metallic character as the energy levels crossed the Fermi level. This may render the metallic behavior of the PS_2 monolayer an extremely appealing anode material for both SIBs and superconductors [162].

4.1.9. Boron sulfide (B₂S)

In their study, Li et al. examined the recently advanced boron sulfide (B_2S) and its potential accessibility as a novel lightweight 2D Dirac anode for SIBs and KIBs using first-principles simulations. It was inferred that B_2S exhibits a high electronic conductivity while acquiring a distinctive "self-doping" impact through the creation of S or B vacancies. The B_2S anode in Na- and K-ion batteries reached extremely high energy densities of 2245 and 1167 mW h g^{-1}, respectively, a function of capacity and OCV designated by conventional hydrogen electrode potential, which is considerably bigger than the energy density of graphene. A further important feature of the B_2S is its graphene-like wettability towards typical electrolytes used SIBs and PIBs, namely, solvent molecules and metal salts, implying outstanding compatibility. Also, the minimum energy path to allow Na- and K-ions to diffuse across the B_2S surface indicates energy barriers of 0.19 and 0.04 eV, respectively, supporting a high level of ionic conductivity. In addition, it was found that ion intercalation causes an insignificant contraction of the B_2S lattice owing to electrode corrugation caused by adsorption, which offsets the dilatation of the lattice. Based on these findings, the B_2S electrode is a suitable lightweight 2D Dirac anode material due to its high energy density, good rate performance, and excellent wettability in the electrolytes [163]. In another attempt, the same material was examined by Li et al. for energy storage applications using DFT studies. B_2S has a planar honeycomb structure, and the simulated lattice constants are found as a = 9.14 Å, b = 5.26 Å, and c = 20.88 Å. The structural stability was confirmed by AIMD, phonon spectra, and linear elastic constants. The B-B and B-S bond lengths equal 1.62 Å and 1.82 Å, respectively. The structure of 2D B_2S is similar to graphene, with the only difference of the larger hexagonal ring. Therefore, B_2S is anticipated to be an efficient anode material useful in Na storage. As SIBs anode, single layer B_2S has a lesser diffusion barrier ∼ 0.23 eV, and fast Na migration, which could promise a fast charge/discharge process. The adsorption of Na content enhanced the metallicity, which is a fascinating factor for battery applications. The high Na storage capacity, such as 1498 mA g h^{-1}, motivates B_2S as an excellent host material for SIBs [164].

4.1.10. Zirconium-, Niobium-, and Chromium- sulfides (ZrS₂, NbS₂, and CrS₂)

Using computational calculations, 2D ZrS_2, NbS_2, and CrS_2 are stable in octahedral (1 T), hexagonal (2H), and distorted octahedral (1 T') due to higher binding energies, respectively. The optimized lattice constants for ZrS_2, NbS_2, and CrS_2 are $a = b = 3.64$ Å, $a = b = 3.31$ Å, and $a = b = 2.55$ Å, individually. The electronic properties of monolayer ZrS_2 and NbS_2 revealed semiconducting properties with energy band gaps of 2.2 eV and 1.22 eV, respectively. However, CrS_2 exhibited metallic nature. As anode materials for SIBs, TiS_2, ZrS_2, NbS_2, and CrS_2, MoS_2 and VS_2 were examined by Yang et al. Among these mateials, TiS_2, ZrS_2, NbS_2 and MoS_2 show average voltage ranges from 0.49 to 0.95 V and specific capacities of 260–339 mA h g^{-1}. The activation barrier for NbS_2 was computed as low as 0.07 eV, showing a fast-cycling rate for Na migration. A strong interaction of Na and the proposed 2D structures was found, which suggests that Na and understudy materials have excellent chemical activity. In terms of average voltage and capacity, M = Ti, Zr, Nb, and Mo are found to be suitable as anodes for sodium ion batteries (SIBs) with voltages of 0.49–0.95 V and theoretical capacities of 260–339 mA h g^{-1}. The high electronic conductivity makes these materials admirable for SIBs [165].

The experimental work of Ou et al. illustrated that NbS_2 nanosheets with layered structures have been fabricated by a facile chemical exfoliation technique and can be serviceable as the anode material. The chemically exfoliated NbS_2 (ce-NbS_2) nanosheets display optimal-rate performance and noticeable cycling stability, which deliver a maximal reversible specific capacity of ∼ 205 mAh g^{-1} at 100 mA g^{-1}. According to the situ X-ray diffraction probing, the ce-NbS_2 nanosheets do not undergo undesirable phase transition during sodiation/desodiation, rendering them attractive for the production of optimal capacity as well

as anode materials with longevity cycle applicable in SIBs [166]. Kim et al. explored the feasibility of applying ZrS_2 as an electrode material candidate in the LIBs, inspired by analogous TiS_2, which is known as the first intercalation compound. ZrS_2 delivers a starting discharging and charging capacity of about 271.8 mAh/g and 166.2 mAh/g, correspondingly, leading to the Coulombic efficiency of 61 %. The largely irreversible capacity loss (43 %, second discharge capacity: 154.6 mAh/g) is attributed to the partial creation of a solid electrolyte interface (SEI) layer or insufficient deintercalation reaction for reverse charge. The reaction related to the conversion reaction begins around 0.3 V, and intercalation and conversion reactions occur simultaneously. It exhibits a higher first discharging e capacity ~ 386.1 mAh/g than the discharging e capacity value obtained in the voltage span from 1.0 to 3.0 V [167]. In Table 1, the electrochemical properties of well-reported 2D MSs are depicted.

4.2. Metal carbides

4.2.1. Vanadium carbide (V_2C)

The structure of monolayer V_2C consists of a hexagonal assembly similar to graphene. Based on the literature, the structure of V_2C is composed of ternary layers, i.e., sandwiched structure. The atoms are stuck in a sequence of V-C-V with bond lengths and atomic thicknesses of 2.00 Å and 2.16 Å, respectively. The optimization of lattice parameters provides $a = b = 2.91$ Å, and the nature of the electronic structure is metallic. Employing first-principle calculations, Li et al. investigated the V_2C monolayer applicable as anode material in SIBs. Its corresponding theoretical capacity was equal to 470.65 mAh g^{-1} and a mean OCV of 0.82 V at $x = 2$ (x is Na content loaded on the V_2C sheet). The charge/discharge process is fast, confirmed via a marginal diffusion barrier of ~ 0.016 eV. These findings reveal that V_2C is an excellent host material for Na storage [172]. Experimentally, sodium fluoride and hydrochloric acid were used for 72 h at 90 °C to efficiently synthesize a new 2D V_2C MXene carbide of high purity from etching V_2AlC. The as-prepared V_2C MXene was > 90 wt% pure that involved only minor impurities, such as $Na_5Al_3F_{14}$ and V_2AlC, as determined by analyses of X-ray diffraction, energy dispersive spectra, and X-ray photoelectron spectroscopy. By utilizing this procedure, V_2C MXene has a higher purity compared to those produced by HF etching at ambient temperature. In as-synthesized form, V_2C MXene demonstrated outstanding electrochemical features promising for anodes based on lithium-ion batteries. By discharging below 370 mA g^{-1}, the capacity can reach 260 mAh g^{-1}. The capacity was boosted by charging at a maximal rate of ~ 500 mA g^{-1} per charge cycle. A high-purity V_2C was inferred as a potential anode material with high performance [173].

4.2.2. Titanium carbides (TiC_3, Ti_3C_2)

Yu et al. employed first-principle calculations to investigate TiC_3, which could be a potential contender as an anode material in SIBs. It

achieved a maximum theoretical capacity of ~ 1278 mAh g^{-1}, greater than commercial anode materials such as graphene. TiC_3 ensures excellent electrical conductivity after loading Na content during the battery cycle. Moreover, the high cohesive energy favors the experimental synthesis of TiC_3. Besides this, the simulated activation barriers for path 1 (A_1-A_2-A_1) and path 2 (A_1-A_1) are 0.18 eV and 0.31 eV, respectively (Fig. 6). These lower energy barriers approve fast Na migration. The average OCV in view of full sodiation was 0.16 V, suggesting that TiC_3 could be an impressive anode material applicable to SIBs [112]. In another attempt, Er et al. [174] studied 2D Ti_3C_2 as an anode material for SIBs using DFT investigations. Monolayer Ti_3C_2 was assembled by removing Al from Ti_3AlC_2. The layers are stuck in the arrangement of Ti(s) − C − Ti(c) − C − Ti(s), in which Ti(s) denotes the Ti atoms' surface, and Ti(c) represents the central Ti atoms in Ti_3C_2. The optimized structural parameters are a = b = 3.1005 Å which agree well with the experimental value [175]. Its average OCV is 0.137 V, with a notable capacity of ~ 351.8 mAh g^{-1}. The low activation barrier for Na (0.096 eV) suggests that Na diffusion in Ti_3C_2 is fast with a high charge/discharge rate.

The synthesizing of Ti_2C MXene nanosheet for high-performance SIBs was done by Wang et al. The presence of Ti_2C MXene is revealed by the TEM images displayed in Fig. 6c-d. As seen in Fig. 6d, following the adsorption of Na, there is a clear expansion after Na loading. The galvanostatic charge/discharge experiments were performed after the confirmation that activated Ti_2CT_x is an encouraging applicant as a negative-electrode for Na-ion hybrid capacitors. At cathode, the Na^+ adsorption/intercalation, while at anode the Na^+ desorption/deintercalation occur. The charge/discharge curves with cutoff voltages of 0.1–3.0 V against Na^+/Na^+ at 20 mA g^{-1} are displayed in Fig. 6e. A voltage plateau at approximately 0.6 V is exhibited by the first charge that transports a large capacity of 360 mAh g-1. A much smaller capacity is exhibited in the given first discharge curve, which has a capacitor-type slope ranging from 0.2 to 2.5 V, which results in a decreased Coulombic efficiency of 65 % for the first cycle. Nevertheless, following the first number of cycles for activation, a stable and efficient electrode performance is exhibited by Ti_2CT_x. A capacitor-type slope between 0.1 and 2.3 V is exhibited by the charge/discharge profiles, with a mean working potential of 1.3 V, which delivers a reversible capacity of about 175 mAh g^{-1} with excellent cycle stability (Fig. 6f illustrates the 12 and 19 % losses of the second capacity after 50 and 100 cycles, correspondingly). The mean operating potential of 1.3 V is large for the utilization as the negative electrode; however, it is advantageous for stable operation, maintaining the capacity at an increased rate and evading the Na metal plating for safety measures. The charge/discharge trends of Ti_2CT are given in Fig. 6g at a range of different specific currents. Despite the high rates of 156 (200 mA g^{-1}), 113 (1000 mA g^{-1}), and 63 mAh g^{-1} (1,000 mA g^{-1}) the reversible capacity is maintained. The rate capabilities of Ti_2CT_x, expanded graphite, hard carbon and $P2$-$Na_{0.66}[Li_{0.22}Ti_{0.78}]O_2$ are compared in Fig. 6h. The capacity preservation at high rates for the

Table 1

2D metal sulfides with their excellent electrochemical performances such as OCV (V), diffusion barrier (eV), and specific capacity (mAh/g)) as anode materials for SIBs.

| Material	OCV	Capacity	Activation barrier	Stable Symmetry	Experimentally available	Ref. No
VS_2	1.30	232.91	0.085	Hexagonal	Yes	[141]
TiS_2	0.9	478	0.13	Trigonal	Yes	[146]
MoS_2	1.0	335	0.11	Hexagonal	Yes	[149]
B_2S	0.48	1498	0.23	Hexagonal	No	[163]
YS_2	1.4	350	0.24	Trigonal	No	[160]
GeS_2	0.23	512	0.09	Tetragonal	Yes	[152]
SiS	0.097	445.6	0.135	Hexagonal	Yes	[158]
SnS_2	1.0	586	0.13	Trigonal	Yes	[155]
CoS_2	0.46	326	0.22	Tetragonal	No	[168]
NbS_2	0.95	275	0.07	Hexagonal	No	[165]
WS_2	0.89	315	0.12	Hexagonal	No	[169]
ReS_2	0.92	428	0.16	Triclinic	No	[165]
PS_2	0.18	1692	0.17	Trigonal	No	[170]
CuS_2	0.64	841	0.20	Octahedral	No	[171]
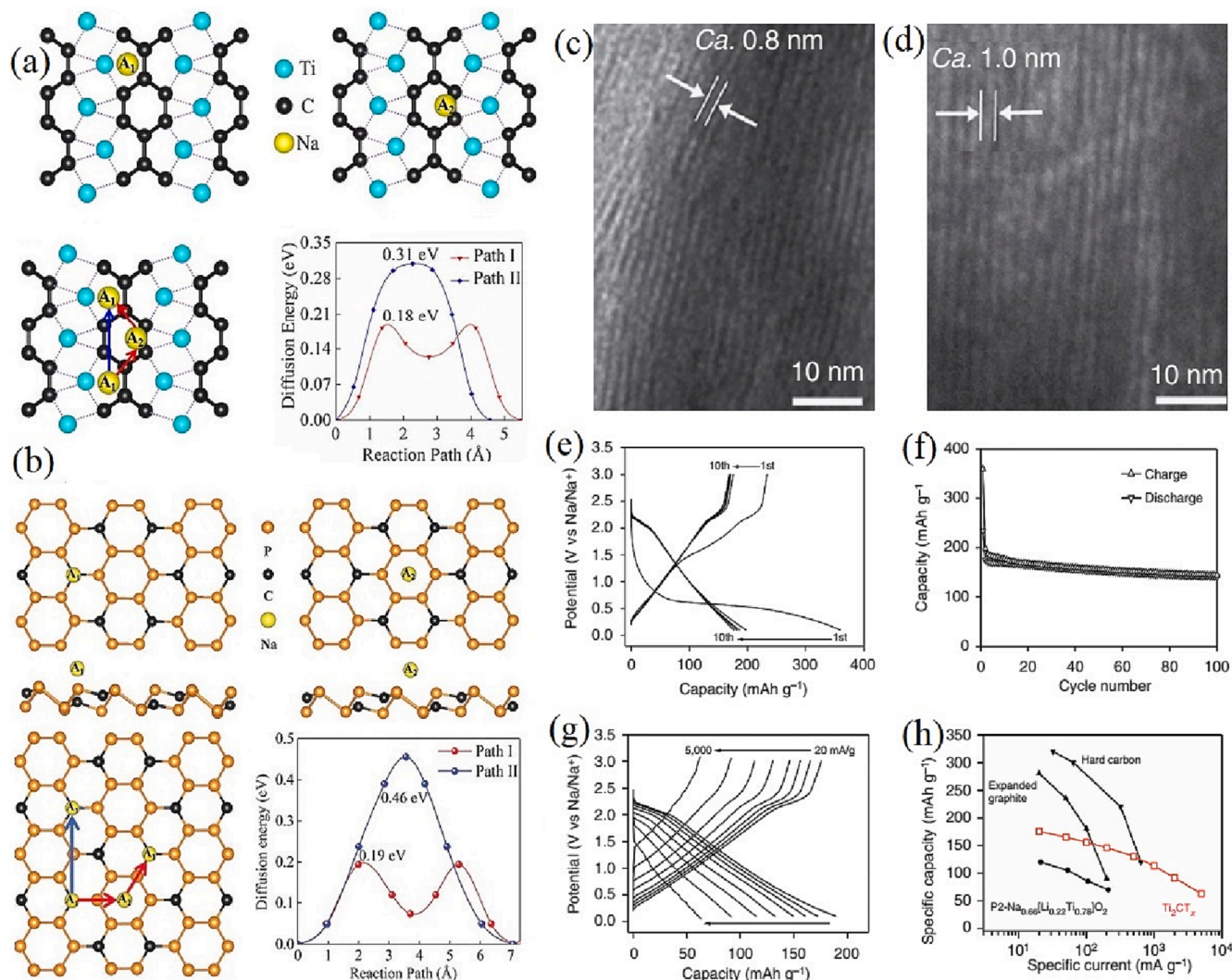
Fig. 6. (a) TiC$_4$ ring with Na adsorbed onto A1, the adsorption of Na at the C$_6$ ring center on A$_2$, the minimum energy paths of Na migration over TiC$_3$ monolayer, and the associated activation barriers for paths I and II. Copyrighted from Ref. [174]. (b) Na adsorption on A1, the top of the underneath C atom. Na adsorbed at the P$_6$ ring center, named A$_2$. The minimum energy paths of Na migration onto P$_3$C, and the associated activation barriers for paths I and II. Copyrighted from Ref. [176]. (c) TEM image of the pristine Ti$_2$CT$_x$. (d) TEM image of activated Ti$_2$CT$_x$ after the first CV. (e-f) Charge/discharge curves and cycle stability for Ti$_2$CT$_x$ in a 1 M NaPF$_6$/EC-DEC electrolyte. The specific current is 20 mA g^{-1} with cut-off voltages in the range of 0.1–3.0 V versus (vs) Na/Na$^+$. (g) Charge/discharge profiles at different rates. (h) Rate capability for Ti$_2$CT$_x$, hard carbon, expanded graphite, and P$_2$-Na$_{0.66}$[Li$_{0.22}$Ti$_{0.78}$]O$_2$. Reproduced for Ref. [177].

carbon compounds (expanded graphite and hard carbon) is smaller than that of Ti$_2$CT$_x$ despite its high capacity of about 300 mAh g^{-1} at a low rate. During the cycle, the electrode material (P$_2$-Na$_{0.66}$[Li$_{0.22}$Ti$_{0.78}$]O$_2$) has no change in lattice volume. Thus, high-capacity retention at large rates is enabled by the minimum structural change related to desodiation. Nevertheless, P$_2$-Na$_{0.66}$[Li$_{0.22}$Ti$_{0.78}$]O$_2$ has a smaller theoretical capacity compared to that of Ti$_2$CT$_x$. An enlarged capacity at any charge/discharge rate is delivered by Ti$_2$CT$_x$. Thus, it is considered a high-performance electrode with increased stability, safety, capacity, and power. It is noteworthy to mention that a 50 mm thick electrode was utilized to obtain the high capability, which makes its practical usage in Na-ion hybrid capacitors extremely realistic [160].

4.2.3. Phosphorous carbides (P$_3$C, PC)

As a potential anode material useful in SIBs, the P$_3$C monolayer has been examined by Zhao et al. employing DFT studies. The low diffusion barriers (0.19 eV, 0.46 eV) (as shown in Fig. 6 (ii)), confirm its high charging/discharging processes. Moreover, the low average OCV, high theoretical capacity (1022 mAh g^{-1}), and excellent mechanical stability are the key characteristics of P$_3$C anode material for SIBs. An attempt

was made by Qi et al. to explore phosphorous carbide (PC) monolayer suitable as anode material in SIBs via DFT calculations. The evaluated mean OCV acquired 0.76 V with a high theoretical capacity of ~ 467.4 mAh g^{-1}. The activation barrier was computed to check the charge/discharge processes, which is 0.25 eV for Na migration. These important features await the confirmation of PC as promising anode material for the SIBs [176].

4.2.4. Molybdynm carbides (MoC, Mo$_2$C, MoC$_2$)

Yu et al. explored single-layer molybdenum carbides with different structures such as MoC, Mo$_2$C, and MoC$_2$ for battery applications by first-principle calculations. The structural parameters for MoC, Mo$_2$C, and MoC$_2$ are ($a = 3.75$ Å, $b = 4.05$ Å), ($a = b = 2.99$ Å), and ($a = 3.03$, $b = 4.84$), respectively. The predicted 2D structures exhibited strong mechanical stabilities, high electronic conductivity, and excellent Na storage performance. The calculated capacity of Na$_2$Mo$_2$C, Na$_2$MoC$_2$, and NaMoC are 262.9 mAh g^{-1} (0.31 V), 466.9 mAh g^{-1} (0.28 V), and 248.2 mg^{-1} (0.80 V), respectively. To investigate the charge/discharge processes, the NEB technique has been applied to find the activation barriers. As shown in Fig. 7, numerous diffusion paths with
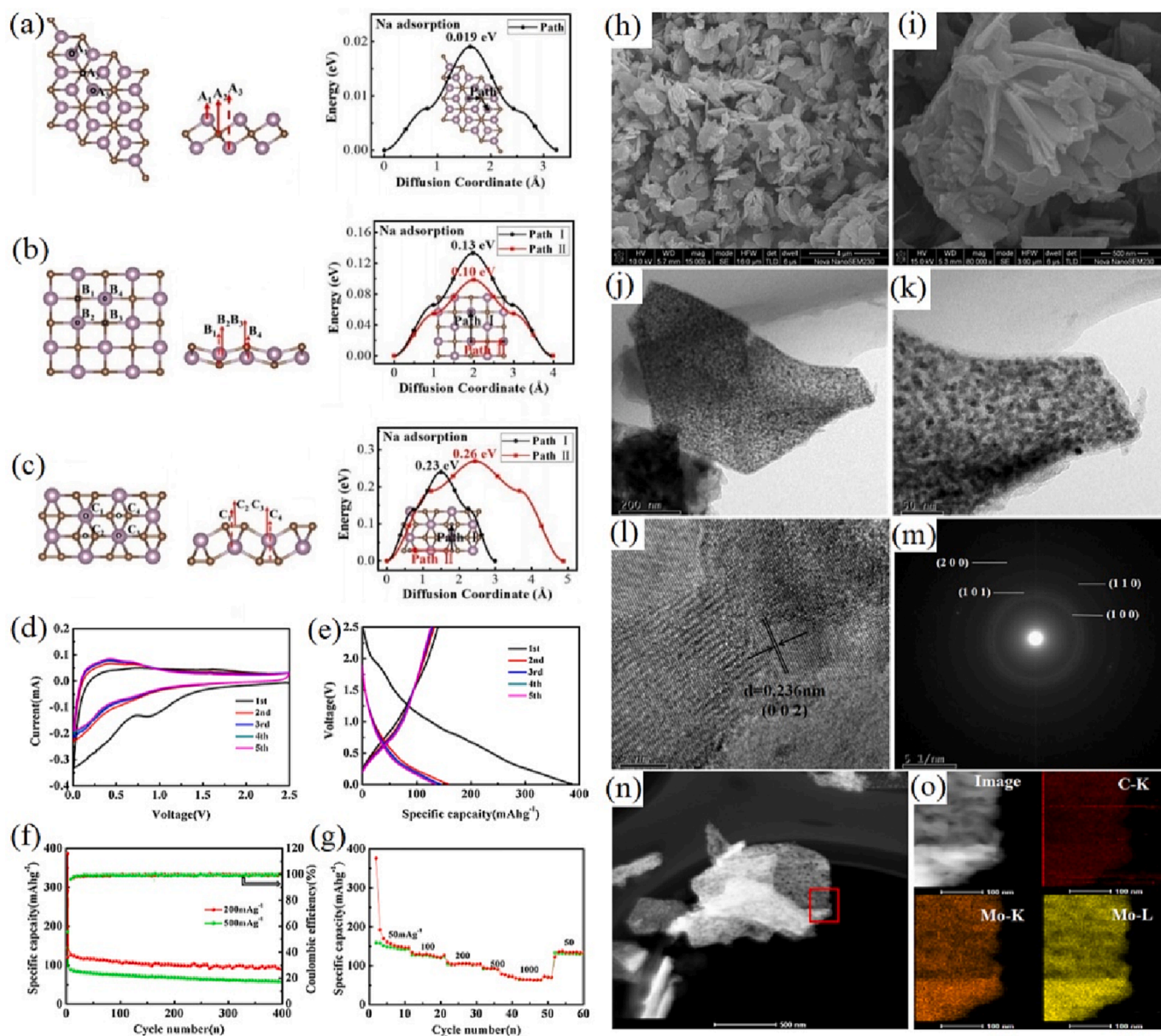
Fig. 7. The high-symmetry adsorbed atomic sites of Na for monolayers (a) Mo_2C and migration paths along with their diffusion energy barriers, (b) MoC and migration paths along with their diffusion energy barriers, and (c) MoC_2 and migration paths along with their diffusion energy barriers. Reproduced from Ref. [178]. Electrochemical characterizations of the Mo_2C nanoplates electrode. (d) Cyclic voltammetry curves of the Mo_2C nanoplates anode for five cycles at a constant scan rate. (e) The initial five charge and discharge curves of the Mo_2C nanoplates electrode at 100 mA g^{-1}. (f) Cycle performances of SIB with Mo_2C nanoplates electrode at 200 and 500 mA g^{-1}, respectively. (g) Rate performance at different current densities. Reproduced from Ref. [179].

corresponding diffusion barriers were calculated. The calculated activation barriers for MoC, Mo_2C, and MoC_2 are plotted in Fig. 7a–c, respectively. The activation barriers are very low, signifying that molybdenum carbide has high charge/discharge rates for Na transfer. Therefore, the predicted three structures could be promising anode materials for the SIBs [178].

Lv and his coworker used a facile strategy in the assembly of Mo_2C nanoplates with ultrafine nanoparticles and amine-metal oxide as the precursor. Longevity, sizeable-rate capability, and longevity are some of the excellent sodium storage features offered by this material if it is utilized as a potential anode that applies to Na-ion batteries. Specifically, the CV profiles of the Mo_2C electrode that are done at a scan rate of 0.2 mV/s between 2.50 and 0.01 V (vs Na/Na +) are shown in Fig. 7 (d). In the first cycle, a broad irreversible peak is seen between 0.7 and 1.0 V, which disappears in the next cycles, which is a result of the production of the solid electrolyte interface (SEI) layer and the

decomposition of the electrolyte. The CV curves overlap in the subsequent cycles. This proves the exceptional stability and high reversibility of the Mo_2C nanoplates at the time of Na ion insertion and extraction. The charge–discharge curves of the Mo_2C nanoplates for the first five cycles at a current of 100 mA/g are displayed in Fig. 7(e), which is in high agreement with the CV curves. Starting discharge-specific capacities of 386.6 mAh g^{-1} are demonstrated by the sample, which quickly decreases to 158.0 mAh g^{-1} in the second cycle. This presents a decreased starting Coulombic efficiency, originating from the intercalation of Na + ions into the interlayer of Mo_2C and the production of the SEI layer. During the next cycles, the specific capacity is reduced slowly, and the Coulombic efficiencies reach 94 % following five cycles. Fig. 7(f) shows the cycling behaviors of the Mo_2C nanoplates at a range of current densities. The capacity persists at 58.1 mAh g^{-1} (500 mA g^{-1}) and 90.8 mAh g^{-1} (200 mA g^{-1}) following 400 cycles, respectively. Moreover, following ten cycles, the Coulombic efficiencies of the Mo_2C nanoplates

electrode are approximately 100 %, which shows a stable cycling performance. The rate performance of the Mo$_2$C nanoplates electrode is given in Fig. 7(g). Reversible capacities of 161.4, 128.2, 105.7, 93.7, and 64.1 mAh g^{-1} at 50, 100, 200, 500, and 1000 mA g^{-1}, correspondingly, are achieved by the Mo$_2$C nanoplates electrode. The capacity of 137.6 mAh g^{-1} is maintained without any noticeable capacity loss when the current density is decreased to 50 mA g^{-1}. This exception electrochemical performance can be linked to its structure, where ultrafine nanoparticles produced Mo$_2$C nanoplates. More surfaces available for the reaction amongst active materials and sodium can be provided by the ultrasmall size of the Mo$_2$C NPs as the small ion diffusion pathway allows for easier and quicker access to Na$^+$. Also, the conductive pathways for efficient charge transfer are ensured by the intimate connection between Mo$_2$C nanoplates. Thus, it is shown that Mo$_2$C is a highly promising anode material that can be utilized in SIBs [179].

4.2.5. Tungston- and Yiterium- carbides (W$_2$C, Y$_2$C)

A freestanding hexagonal (2H phase) W$_2$C was explored computationally for SIBs by Samad et al. The relaxed structure has lattice parameters, referred to as $a = b = 2.84$ Å, with the W-C bond length equal to 2.15 Å. The high in-plane stiffness (278 N m^{-1}), formation energy, metallicity, and phonon spectrum confirm its structural stability, as shown in Fig. 9(I). As an anode material for SIBs, it has intrinsic metallic nature, strong mechanical strength, and high Na adsorption. The OCV profile (0.88–0.38 V) is in the market anode materials window with a Na storage capacity of 113 mAh g^{-1}. To find the charging/discharging rates, the energy surface for Na migration was calculated by nudged elastic band (NEB) technique. The simulated diffusion barrier for the minimum energy path is 0.019 eV. These outcomes reveal that monolayer W$_2$C is an excellent host material for SIBs with an ultralow sodium diffusion barrier [180]. Hou et al. theoretically reported Y$_2$C monolayer as an anode material for SIBs. 2D Y$_2$C electrode has strong in-plane stiffness. After relaxation, the relaxed lattice constants are determined as $a = b = 3.578$ Å, and the Y-C bond length equals 2.464 Å. The geometry of Y$_2$C is stable in the trigonal phase, confirmed by phonon dispersion and higher binding strength. DOS results of pristine Y$_2$C revealed metallic nature. Its excellent electronic conductivity is sustainable after the adsorption of Na content. The maximal theoretical specific capacity (564 mAh g^{-1}) and the small mean OCV (0.24 V) affirmed the potential usefulness of a single-layer Y$_2$C electrode for Na storage. The charge/discharge process was estimated via the procedure to find diffusion barriers and the corresponding pathways. Three paths were chosen, such as path 1 (C-Y$_B$-C), path 2 (C—C), and path 3 (C-Y$_T$-C) attained the corresponding energy barriers around 0.01 eV, 0.01 eV, and 0.11 eV. Since the activation barriers are quite low, the Y$_2$C electrode discloses high sodiation/desodiation rates [89].

4.2.6. Silicon- and Tin-carbides (SiC, SnC)

Hosseinian et al. investigated the properties of 2D SiC beneficial as anode material in SIBs employing DFT calculations. The structure of SiC is similar to graphane with lattice constants a = b = 3.09 Å and bond length Si-C = 1.48 Å. Monolayer pristine SnC has semiconducting behavior while it revealed metallic character after the adsorption small of Na content. A strong interaction was seen between SiC and Na. The low voltage profile exhibited a maximum theoretical capacity of 668 mAh g^{-1} [181,182]. In another report, Wang et al. explored single-layer silicon carbide (Si$_3$C) for energy storage purposes using computational simulations. The assembly of 2D Si$_3$C is a planner with structural parameters $a = b = 7.02$ Å. Si-C and Si-Si bond lengths are 1.81 Å and 2.25 Å, respectively. As anode material for SIBs, the calculated diffusion barrier for Na migration is 0.34 eV, revealing high charge/discharge processes [183]. Experimentally, it is challenging to synthesize SiC monolayer. However, an approach is made by Kumari et al. to prepare nano SiC cubic architecture for Li insertion. Anode materials for LIBs demonstrated maximal capacity and lengthy cycling. During 200 cycles, a capacity of over 1200 mAh g^{-1} was observed for the reversible insertion of lithium [184].

With the use of DFT simulations, But et al. examined the structural, electrochemical, and electronic behaviors of SnC monolayer convenient for anodic purposes. For the pristine SnC single-layer, the electronic structure shows an indirect-gap semiconducting behavior. Its corresponding bandgaps are 1.72 eV and 0.92 eV, respectively, according to HSE06 and GGA-PBE calculations. The semi-metallic transition is detected when a low amount of Na is inserted. Also, the SnC monolayer has a small OCV of 0.24 V and a theoretical capacity of ~ 205 mA g h^{-1}. The prompt charging-discharging mechanism is facilitated by the weak diffusion barrier of 0.17 eV. Based on the results of this analysis, SnC monolayers could serve as an efficient anode material applicable to SIBs [185].

4.2.7. Scandium carbide (ScC$_2$)

2D ScC$_2$ was reported by Huang et al. for SIBs applications via first-principles calculations. The ScC$_2$ nanosheet possesses an orthogonal geometry with *the Pmmn* space group analogous to the geometries of TiC$_2$, YN$_2$, and FeC$_2$ sheets. The primitive cell of ScC$_2$ contains four carbon and two scandium atoms. Monolayer ScC$_2$ has three polymorphs hexagonal (H), tetragonal (T), and orthogonal (o). The most stable one is orthogonal (o-ScC$_2$), and the corresponding lattice parameters are $a = 5.39$ Å and $b = 4.12$ Å. Based on DFT calculations, bare o-ScC$_2$ is conductive, i.e., metallic. It was noticed that monolayer ScC$_2$ has thermal stability, and it exhibits a metallic nature over the sodiation procedures. The determined average OCV is 0.08 V, along with an optimal theoretical capacity of 777 mAh g^{-1}. Moreover, the simulated activation barrier for Na migration is 0.05 eV, revealing fast charge/discharge processes. The low diffusion barrier, low average OCV, thermal stability, and the significant specific capacity of ScC$_2$ make it a suitable anode material in SIBs [186]. In another report, Lv et al. investigated 2D ScC$_2$ using first-principles calculations. With the use of anode material in SIBs, 2D ScC$_2$ conveyed a maximum capacity of 362 mAh g^{-1} with a mean OCV of 0.24 V. The high electronic conductivity and low activation barrier (0.012 eV) revealed a fast charge/discharge process. These excellent features compel monolayer ScC$_2$ as a promising Na host material [187].

4.2.8. Nickel-carbides (NiC$_3$)

Zhu et al. conducted first-principles calculations to examine 2D NiC$_3$ as a high-storage anode material for SIBs. Using PBE functional, the optimized unit cell of NiC$_3$ monolayer contains 12C atoms and four Ni atoms, while lattice constants are $a = 11.22$ Å and $b = 4.36$ Å. Each Ni atom binds with four C atoms directly neighboring it to constitute four Ni-C bonds, while their associated distances are 1.97 Å and 1.99 Å, respectively. The adjacent Ni-Ni distance is equal to 2.24 Å. The planner NiC$_3$ has superb cohesive energy, strong mechanical stability, positive phonon mode, and significant thermal stability. Based on *ab initio* investigations, the electronic nature of 2D NiC$_3$ is metallic. In contrast, the metallicity was boosted via Na-doped orthogonal ScC$_2$ and ScN$_2$ sheets useful as striking anode materials in SIBs, which is beneficial for electrochemical performance. Its average OCV is very low (0.17 V) and has a superior theoretical capacity of ~ 1698 mAh g^{-1}. The calculated diffusion barrier is low (0.23 eV), suggesting that monolayer TiC$_3$ is a high charging/discharging host material for SIBs [188].

4.2.9. Niobium carbide (Nb$_2$C)

In a report, Hu et al. simulated single-layer Nb$_2$C for anodic applications. According to their calculations, the optimization of lattice parameters is $a = b = 6.302$ Å, and the thickness (distance between layers) is equal to 2.468 Å along with a bond length (Nb-C) of about 2.198 Å. Nb$_2$C is metallic before and after Na loading. The calculated average OCV is very low, 0.27 V, with a Na storage capacity of 271 mAh g^{-1}. Moreover, the activation barriers (0.004 eV, 0.015 eV) for the two paths are much lower, showing high charging/ discharging rates [189]. Zhao et al. produced 2D few-layer niobium carbide (Nb$_2$CT$_x$) MXene

nanosheets by etching Nb$_2$AlC powder in the first demonstration of a one-step technique. Using the few-layer Nb$_2$CT$_x$ electrode, the sample exhibits a maximal specific capacity of ~ 354 mAh g^{-1}, providing a longer cycling lifetime at 0.05 A g^{-1}. It is feasible to stabilize the specific capacity at 225 mAh g^{-1} following 800 cycles when operating at 1.0 Ag^{-1}. Nb$_2$CT$_x$ MXene nanosheets fabricated by unassisted one-step preparation offer a promising platform for exploring Nb$_2$CT$_x$ -based composite materials and their applications [190]. The preparation of novel 2D niobium and vanadium carbides was reported recently by selectively etching Al from Nb$_2$AlC and V$_2$AlC, correspondingly, at room temperature. In establishing their ability to deal with maximal charging-discharging rates, these novel materials could be advantageous electrode materials for LIBs. Observations indicate that electrodes based on Nb$_2$C and V$_2$C exhibited reversible capacities of 170 and 260 mAh g^{-1} at 1C and 110 and 125 mAh g^{-1} at 10C, respectively [191].

The electrochemical performance of NbC was explored experimentally and theoretically for SIBs by Wang et al. In order to understand the electrochemical mechanism, the electronic characteristics of NbC are found by the application of DFT calculations. Nb(s)-C-Nb(c) stacking sequence is seen in the structure of NbC, as shown in Fig. 8a. Nb(s)
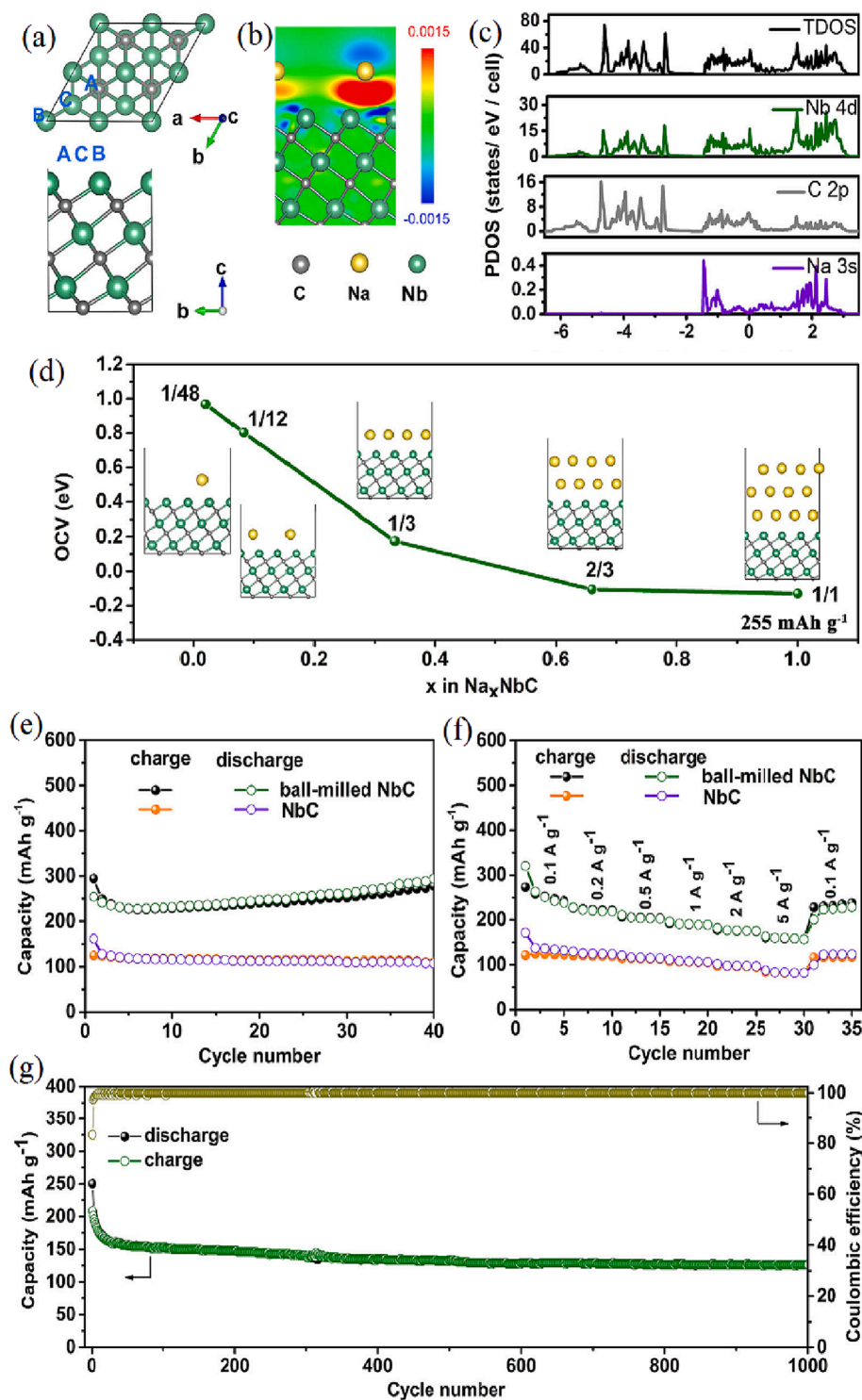

Fig. 8. (a) Diagram showing top and side outlooks of the NbC crystal structure and the possible adsorption sites of Na. (b) Bonding charge density for Na at the C site in the NbC system (isovalue = 0.0015). (c) TDOS and PDOS of Na 1/12NbC. (d) OCV as a function of × in NaxNbC. (e) Cycling performance of bulk NbC and ball-milled NbC at 0.1 A/g. (f) Rate performance of bulk NbC and ball-milled NbC at various current densities. (g) Cycling performance and corresponding Coulombic efficiency of ball-milled NbC at 5 A/g. Reprinted from Ref [192].

denotes the surface Nb atoms, while Nb(c) denotes the center Nb atoms in NbC. The investigation involves a single Na being boned on the $2 \times 2 \times 1$ NbC. The surface has three high-symmetry adatom sites named A, B, and C. Further, A denotes Na bonded on top of the C atom in NbC. B denotes Na bonded on the Nb atom in the upper layer of NbC. Finally, C denotes Na bonded on top of the Nb atom in the middle layer of the NbC, which is the utmost desirable site for Na. The bonding charge density, the projected density of states (PDOS), and the total density of states (TDOS) are found for the adsorption of Na on-site C to achieve more insight into the influence of adatom adsorption on NbC. The bonding charge density in the plane, which passes inside the Na and the high-symmetry line of NbC is shown in Fig. 8b. A charge transfer from the Na to the NbC is revealed by the observed areas of electron density accumulation and depletion, which are shown in red and blue, respectively. Fig. 8c reveals a DOS which portrays a high overlap between the Na_3s orbital and the Nb_4d orbital at 1.50–0.80 eV below the Fermi level. This indicates the s-d hybridization and the sturdy binding of Na on the NbC surface. In addition, as seen in Fig. 8d, the variation in $\times$ in the Na_xNbC system is used to evaluate the OCV as the function of the concentration. stoichiometries of $Na_1/48NbC$, $Na_1/12NbC$, $Na_1/3NbC$, $Na_2/3NbC$, and NaNbC in a $2 \times 2 \times 1$ supercell are correspondant to the $\times$ values of 1/48, 1/12, 1/3, 2/3, and 1/1, respectively. The OCVs are −0.11 and −0.13 V as the content of Na inclines towards 2/3 and 1/1, respectively. The corresponding cycling curves of ball-milled NbC and bulk NbC are displayed in Fig. 8e. The starting charge and discharge capacities of ball-milled NbC are 307 and 242 mAh g^{-1}, individually, which results in a Coulombic efficiency of 79 %. The production of SEI film is the ascription for the irreversible capacity. Following forty cycles, the charge capacity rises to 262 mAh g^{-1}, which corresponds to the reversible production of activated polymer gel-like film on the surface of the active materials at the time of the discharge–charge process. Fig. 8f shows the rate performance of ball-milled NbC and bulk NbC at a range of current densities between 0.1 and 5 A g^{-1}. At current densities of 0.1, 0.2, 0.5, 1, 2, and 5 A g^{-1}, the bulk NbC can attain a charge capacity of 122, 121, 114, 107, 97, and 83 mAh g^{-1}, respectively. Following the cycling at increased current density, the capacity can reduce to 116 mAh g^{-1} at 0.1 A g^{-1}. On the other hand, ball-milled NbC can attain a charge capacity of 273, 226, 207, 193, 178, 160, and 228 mAh g^{-1} for the same current densities, respectively. Furthermore, reversible capacities of 208 and 126 mAh g^{-1} are exhibited by ball-milled NbC for the first and one-thousandth cycles at an increased current density of 5 A g^{-1}, respectively. As seen in Fig. 8g, following the first cycle, the Coulombic efficiency is kept at 100 %. Thus, the electrochemical outcomes display the exceptional cycling and rate performance of NbC electrodes [192]. The voltage, capacity, and activations, barriers of the predicted 2D MCs are given in Table 2.

4.2.10. Manganese carbides (MnC)

MnC monolayer was predicted from DFT, 2D pristine hexagonal manganese carbide (h-MnC) sheet with a wide half-metallic gap near the Fermi energy level. Besides, the h-MnC sheet can keep its structure up to 1000 K, specifying a high thermal stability [193]. In another theoretical framework, Chen et al. examined the MnC monolayer as an anode material for SIBs. Pristine MnC is metallic, which is a good choice for battery applications. Monolayer MnC acquired negative adsorption energy of about − 2.83 eV for Na based on the computational findings. Moreover, MnC has a comparable theoretical capacity of 475 mAh g^{-1} for SiBs. The high adsorption energies, moderate average OCV, and maximum theoretical capacity are the potential features of 2D MnC for Na storage [194]. The systhesis methods and cycle performance of 2D MCs and MSs are given in Table 3.

5. Conclusions and future perspectives

The anode materials for high-performance SIBs are expected to be safe, highly abundant, inexpensive, and have superior energy density. The engineering of 2D materials has spread their application as high-quality host materials for SIBs because of the economical price and maximal theoretical capacity. 2D MSs and MCs groups with layered structures increase Na accommodating sites, lower the Na activation barrier, and possess a high capacity. Thus, 2D MCs and MSs as anode material for SIBs endow a maximal charge/discharge process,

Table 3

The systhesis methods and cycle performance of 2D MCs and MSs.

Material	Synthesis method	Cycle performance	References
VS$_2$ nanosheets	Solvothermal	532/30th/50	[143]
TiS$_2$ nanosheets	Facile method	386/200th/200	[147]
MoS$_2$@ hierarchical porous carbon (MHPC)	Scalable method	732/300th/1000	[151]
GeS$_2$ nanosheets	Facile method	1335/200th/150	[154]
ultrathin GeS$_2$ nanosheets	Topochemical conversion route	515/2000th/10000	[153]
SnS@graphene	Hydrothermal process	940/250th/850	[157]
SnS$_2$/RGO	Hydrothermal process	841/100th/100	[161]
NbS$_2$ nanosheets	Chemical exfoliation	205/1st /100	[166]
C-Ge/C	Facile method	1720/50th /320	[200]
Mo$_2$C nanoplates	Hydrolysis method	90.8/400th/200	[179]
V$_2$C	Etching method	60.08/100th/1000	[201]
2D Nb$_2$CT$_x$	Etching method	225/800th/1000	[190]
NbC	Ball milling	126/1000th/5000	[192]

Table 2

Activation barriers (eV), voltage profiles (V), and Na storage capacity (mAh/g) of some well-known MCs as anode material for SIBs batteries.

Material	OCV	Capacity	Activation barrier	Stable symmetry	Experimentally available	Ref. No
GeC	0.14	633	0.06	Planar	No	[195]
TiC$_3$	1.0	1278	0.18	C$_2$/m	No	[112]
MnC	0.73	475	0.174	Hexagonal	No	[194]
W$_2$C	0.63	144	0.019	Hexagonal	No	[196]
SnC	0.24	205	0.17	Hexagonal	No	[185]
ZrC$_2$	0.41	932	0.02	Pmmm	No	[197]
ScC$_2$	0.08	777	0.05	orthogonal	No	[186]
Nb$_2$C	0.27	271	0.004	Trigonal	No	[189]
Y$_2$C	0.24	564	0.01	Trigonal	No	[89]
NiC$_3$	0.17	1698	0.23	CMMM	No	[188]
P$_3$C	0.582	1022	0.19	R3m	No	[198]
MoC$_2$	0.28	466.9	0.23	Pmmm	No	[178]
Si$_3$C	0.50	1115	0.34	R3m	No	[199]
V$_2$C	0.82	470.65	0.016	Trigonal	Yes	[172]

outstanding capability, and stable cycling performance.

This review discusses the nature and developments of SIBs, detailed computational methods to study electrode materials for SIBs, and the successful application of monolayer MSs and MCs including MoS_2, TiS_2, SnS_2, VS_2, Mo_2C, Nb_2C, Ti_3C_2, etc. Both computational and experimental approaches have been introduced that have been used to explore MSs and MCs as host materials in SIBs. Moreover, this review highlights the structural chemistry of MSs and MCs and Na storage processes in 2D MSs and MCs. The layered structures of MSs and MCs can enhance the Na adsorption and storage capacity because of the surface of a large area and plenty of accommodating atomic sites.

Although significant progress in 2D MSs and MCs nanosheets as Na host materials has been achieved for battery applications, the commercialization of these anodes is still challenging for practical applications. For instance, some 2D MCs and MSs anodes display high Na storage capacity but may cause volume change, including poor conductivity, high cost, and so on. Furthermore, the layered structures have a high interfacial area, which may induce more side reactions that impact the performance of SIBs. The manufacturing of 2D MSs and MCs as Na host materials with outstanding electrochemical performance but less volume change and side reactions is urgently required for the real commercialization of SIBs. Therefore, it is expected that based on synthetic methods, electrochemical mechanisms, and practical morphology design of 2D MCs and MSs would further facilitate the commercialization of SIBs shortly.

Declaration of Competing Interest

The authors declare that they have no known competing financial interests or personal relationships that could have appeared to influence the work reported in this paper.

Data availability

Data will be made available on request.

Acknowledgment

References

[1] H. Kang, Y. Liu, K. Cao, Y. Zhao, L. Jiao, Y. Wang, H. Yuan, Update on anode materials for Na-ion batteries, J. Mater. Chem. A 3 (2015) 17899–17913, https://doi.org/10.1039/C5TA03181H.

[2] D. Deng, M.G. Kim, J.Y. Lee, J. Cho, Green energy storage materials: Nanostructured TiO2 and Sn-based anodes for lithium-ion batteries, Energy Environ. Sci. 2 (2009) 818–837, https://doi.org/10.1039/B823474D.

[3] J.Y. Li, Q. Xu, G. Li, Y.X. Yin, L.J. Wan, Y.G. Guo, Research progress regarding Si-based anode materials towards practical application in high energy density Li-ion batteries, Mater. Chem. Front. 1 (2017) 1691–1708, https://doi.org/10.1039/C6QM00302H.

[4] K.S. Chen, I. Balla, N.S. Luu, M.C. Hersam, Emerging opportunities for two-dimensional materials in lithium-ion batteries, ACS Energy Lett. 2 (2017) 2026–2034, https://doi.org/10.1021/acsenergylett.7b00476.

[5] M.R. Lukatskaya, B. Dunn, Y. Gogotsi, Multidimensional materials and device architectures for future hybrid energy storage, Nat. Commun. 7 (2016) 1–13, https://doi.org/10.1038/ncomms12647.

[6] M.K. Butt, J. Rehman, Z. Yang, S. Wang, A. Elzatahry, A. Alofi, M.D. Albaqami, R. Alotabi, A. Laref, K. Jin, Storage of Na in 2D SnS for Na ion batteries: a DFT prediction, Phys. Chem. Chem. Phys. 24 (2022) 29609–29615, https://doi.org/10.1039/D2CP02780A.

[7] L. Shi, T. Zhao, Recent advances in inorganic 2D materials and their applications in lithium and sodium batteries, J. Mater. Chem. A. 5 (2017) 3735–3758, https://doi.org/10.1039/C6TA09831B.

[8] X. Zeng, M. Li, D. Abd El-Hady, W. Alshitari, A.S. Al-Bogami, J. Lu, K. Amine, Commercialization of lithium battery technologies for electric vehicles, Adv. Energy Mater. 9 (2019) 1900161, 10.1002/aenm.201900161.

[9] J. Zheng, S. Myeong, W. Cho, P. Yan, J. Xiao, C. Wang, J. Cho, J.G. Zhang, Li-and Mn-rich cathode materials: challenges to commercialization, Adv. Energy Mater. 7 (2017) 1601284, https://doi.org/10.1002/aenm.201601284.

[10] Y. Xiao, S.H. Lee, Y.K. Sun, The application of metal sulfides in sodium ion batteries, Adv. Energy Mater. 7 (2017) 1601329, https://doi.org/10.1039/C8TA03444C.

[11] D. Deng, Li-ion batteries: basics, progress, and challenges, Energy Sci. Eng. 3 (2015) 385–418, https://doi.org/10.1002/ese3.95.

[12] G. Assat, J.M. Tarascon, Fundamental understanding and practical challenges of anionic redox activity in Li-ion batteries, Nat. Energy 3 (2018) 373–386, https://doi.org/10.1038/s41560-018-0097-0.

[13] P. Albertus, S. Babinec, S. Litzelman, A. Newman, Status and challenges in enabling the lithium metal electrode for high-energy and low-cost rechargeable batteries, Nat. Energy 3 (2018) 16–21, https://doi.org/10.1038/s41560-017-0047-2.

[14] A.C. Luntz, J. Voss, K. Reuter, Interfacial challenges in solid-state Li ion batteries, J. Phys. Chem. Lett. 22 (2015) 4599–4604, https://doi.org/10.1021/acs.jpclett.5b02352.

[15] S. Sripad, V. Viswanathan, Evaluation of current, future, and beyond Li-ion batteries for the electrification of light commercial vehicles: challenges and opportunities, J. Electrochem. Soc. 164 (2017) E3635, https://doi.org/10.1149/2.0671711jes.

[16] T. Placke, A. Heckmann, R. Schmuch, P. Meister, K. Beltrop, M. Winter, Perspective on performance, cost, and technical challenges for practical dual-ion batteries, Joule 2 (2018) 2528–2550, https://doi.org/10.1016/j.joule.2018.09.003.

[17] J. Rehman, X. Fan, A. Samad, W. Zheng, Lithiation and sodiation of hydrogenated silicene: a density functional theory investigation, ChemSusChem 14 (2021) 5460–5469, https://doi.org/10.1002/cssc.202101742.

[18] J. Rehman, X. Fan, A. Laref, W. Zheng, Adsorption and diffusion of potassium on 2D SnC sheets for potential high-performance anodic applications of potassium-ion batteries, ChemElectroChem 7 (2020) 3832–3838, https://doi.org/10.1002/celc.202001039.

[19] J. Rehman, X. Fan, W. Zheng, Computational insight of monolayer SnS2 as anode material for potassium ion batteries, Appl. Surf. Sci. 496 (2019), 143625, https://doi.org/10.1016/j.apsusc.2019.143625.

[20] I. Sultana, M.M. Rahman, Y. Chen, A.M. Glushenkov, Potassium-ion battery anode materials operating through the alloying–dealloying reaction mechanism, Adv. Funct. Mater. 28 (2018) 1703857, https://doi.org/10.1002/adfm.201703857.

[21] S. Lee, G. Kwon, K. Ku, K. Yoon, S.K. Jung, H.D. Lim, K. Kang, Recent progress in organic electrodes for Li and Na rechargeable batteries, Adv Mater 30 (2018) 1704682, https://doi.org/10.1002/adma.201704682.

[22] J. Cui, S. Yao, J.K. Kim, Recent progress in rational design of anode materials for high-performance Na-ion batteries, Energy Storage Mater. 7 (2017) 64–114, https://doi.org/10.1016/j.ensm.2016.12.005.

[23] M.K. Butt, V.A. Dinh, H.M. Zeeshan, Z. Yang, S. Wang, K. Jin, SnSe2 monolayer is a promising Na host material: A DFT study, Mater. Sci. Semicond. Process. 136 (2021), 106175, https://doi.org/10.1016/j.mssp.2021.106175.

[24] M.K. Butt, J. Rehman, A.S. Alofi, Z. Yang, H.M. Zeeshan, S. Wang, A. Laref, M. D. Albaqami, R.G. Alotabi, J. Kexin, Investigating the electrochemical properties of SnO monolayer in sodium-ion batteries, J Phys Chem Solids. 171 (2022), 110975, https://doi.org/10.1016/j.jpcs.2022.110975.

[25] W. Nie, H. Cheng, X. Liu, Q. Sun, F. Tian, W. Yao, S. Liang, X. Lu, J. Zhou, Surface organic nitrogen-doping disordered biomass carbon materials with superior cycle stability in the sodium-ion batteries, J. Power Sources 522 (2022), 230994, https://doi.org/10.1016/j.jpowsour.2022.230994.

[26] S. Qiu, L. Xiao, M.L. Sushko, K.S. Han, Y. Shao, M. Yan, X. Liang, L. Mai, J. Feng, Y. Cao, Manipulating adsorption–insertion mechanisms in nanostructured carbon materials for high-efficiency sodium ion storage, Adv. Energy Mater. 7 (2017) 1700403, https://doi.org/10.1002/aenm.201700403.

[27] X. Feng, M. Ouyang, X. Liu, L. Lu, Y. Xia, X. He, Thermal runaway mechanism of lithium ion battery for electric vehicles: a review, Energy Storage Mater. 10 (2018) 246–267, https://doi.org/10.1016/j.ensm.2017.05.013.

[28] F.A. Rasmussen, K.S. Thygesen, Computational 2D materials database: electronic structure of transition-metal dichalcogenides and oxides, J. Phys. Chem. C. 119 (2015) 13169–13183, https://doi.org/10.1021/acs.jpcc.5b02950.

[29] J. Xu, J. Dou, Z. Wei, J. Ma, Y. Deng, Y. Li, H. Liu, S. Dou, Recent progress in graphite intercalation compounds for rechargeable metal (Li, Na, K, Al)-ion batteries, Adv. Sci. 4 (2017) 1700146, https://doi.org/10.1002/advs.201700146.

[30] H. Kim, H. Kim, Z. Ding, M.H. Lee, K. Lim, G. Yoon, K. Kang, Recent progress in electrode materials for sodium-ion batteries, Adv. Energy Mater. 6 (2016) 1600943, https://doi.org/10.1002/aenm.201600943.

[31] M.A. Munoz-Marquez, D. Saurel, J.L. Gomez-Camer, M. Casas-Cabanas, E. Castillo-Martinez, T. Rojo, Na-ion batteries for large scale applications: a review on anode materials and solid electrolyte interphase formation, Adv. Energy Mater. 7 (2017) 1700463, https://doi.org/10.1002/aenm.201700463.

[32] X. Zhang, Z. Zhang, Z. Zhou, MXene-based materials for electrochemical energy storage, J. Energy Chem. 27 (2018) 73–85, https://doi.org/10.1016/j.jechem.2017.08.004.

[33] J. Rehman, X. Fan, W. Zheng, 2D SnC sheet with a small strain is a promising Li host material for Li-ion batteries, Mater. Today Commun. 26 (2021), 101768, https://doi.org/10.1016/j.mtcomm.2020.101768.

[34] R. Mas-Balleste, C. Gomez-Navarro, J. Gomez-Herrero, F. Zamora, 2D materials: to graphene and beyond, Nanoscale 3 (2011) 20–30, https://doi.org/10.1039/C0NR00323A.

[35] A. Gupta, T. Sakthivel, S. Seal, Recent development in 2D materials beyond graphene, Prog. Mater. Sci. 73 (2015) 44–126, https://doi.org/10.1016/j.pmatsci.2015.02.002.

[36] X. Liu, J.Q. Huang, Q. Zhang, L. Mai, Nanostructured metal oxides and sulfides for lithium–sulfur batteries, Adv. Mater. 29 (2017) 1601759, https://doi.org/10.1002/adma.201601759.

[37] F. Li, Z. Wei, A. Manthiram, Y. Feng, J. Ma, L. Mai, Sodium-based batteries: from critical materials to battery systems, J. Mater. Chem A. 7 (2019) 9406–9431, https://doi.org/10.1039/C8TA11999F.

[38] R. Frisenda, E. Navarro-Moratalla, P. Gant, D.P. De Lara, P. Jarillo-Herrero, R. V. Gorbachev, A. Castellanos-Gomez, Recent progress in the assembly of nanodevices and van der Waals heterostructures by deterministic placement of 2D materials, Chem. Soc. Rev. 47 (2018) 53–68, https://doi.org/10.1039/C7CS00556C.

[39] Z. Lin, Y. Lei, S. Subramanian, N. Briggs, Y. Wang, C.-L. Lo, E. Yalon, D. Lloyd, S. Wu, K. Koski, Research update: recent progress on 2D materials beyond graphene: from ripples, defects, intercalation, and valley dynamics to straintronics and power dissipation, APL Mater. 6 (2018), 080701, https://doi.org/10.1063/1.5042598.

[40] S. Zhang, S. Guo, Z. Chen, Y. Wang, H. Gao, J. Gómez-Herrero, P. Ares, F. Zamora, Z. Zhu, H. Zeng, Recent progress in 2D group-VA semiconductors: from theory to experiment, Chem. Soc. Rev. 47 (2018) 982–1021, https://doi.org/10.1039/C7CS00125H.

[41] M.I. Jamesh, A. Prakash, Advancement of technology towards developing Na-ion batteries, J. Power Sources. 378 (2018) 268–300, https://doi.org/10.1016/j.jpowsour.2017.12.053.

[42] V. Palomares, P. Serras, I. Villaluenga, K.B. Hueso, J. Carretero-González, T. Rojo, Na-ion batteries, recent advances and present challenges to become low cost energy storage systems, Energy Environ. Sci. 5 (2012) 5884–5901, https://doi.org/10.1039/C2EE02781J.

[43] A. Eftekhari, D.W. Kim, Sodium-ion batteries: new opportunities beyond energy storage by lithium, J. Power Sour. 395 (2018) 336–348, https://doi.org/10.1016/j.jpowsour.2018.05.089.

[44] D.L. Cheng, L.C. Yang, M. Zhu, High-performance anode materials for Na-ion batteries, Rare Metals 37 (2018) 167–180, https://doi.org/10.1007/s12598-018-1015-0.

[45] H. Zhang, I. Hasa, S. Passerini, Beyond insertion for na-ion batteries: nanostructured alloying and conversion anode materials, Adv. Energy Mater. 8 (2018) 1702582, https://doi.org/10.1002/aenm.201702582.

[46] H. Fu, Y.-P. Wang, G. Fan, S. Guo, X. Xie, X. Cao, B. Lu, M. Long, J. Zhou, S. Liang, Synergetic stability enhancement with magnesium and calcium ion substitution for Ni/Mn-based P2-type sodium-ion battery cathodes, Chem. Sci. 13 (2022) 726–736, https://doi.org/10.1039/D1SC05715D.

[47] W. Kang, N. Deng, J. Ju, Q. Li, D. Wu, X. Ma, L. Li, M. Naebe, B. Cheng, A review of recent developments in rechargeable lithium–sulfur batteries, Nanoscale. 8 (2016) 16541–16588, https://doi.org/10.1039/C6NR04923K.

[48] X. Cao, C. Tan, X. Zhang, W. Zhao, H. Zhang, Solution-processed two-dimensional metal dichalcogenide-based nanomaterials for energy storage and conversion, Adv. Mater. 28 (2016) 6167–6196, https://doi.org/10.1002/adma.201504833.

[49] S. Sun, C. Liao, A.M. Hafez, H. Zhu, S. Wu, Two-dimensional MXenes for energy storage, J. Chem. Eng. 338 (2018) 27–45, https://doi.org/10.1016/j.cej.2017.12.155.

[50] K. Khan, A.K. Tareen, M. Aslam, A. Mahmood, Y. Zhang, Z. Ouyang, Z. Guo, H. Zhang, Going green with batteries and supercapacitor: two dimensional materials and their nanocomposites based energy storage applications, Prog. Solid. State Ch. 58 (2020), 100254, https://doi.org/10.1016/j.progsolidstchem.2019.100254.

[51] E. Singh, K.S. Kim, G.Y. Yeom, H.S. Nalwa, Two-dimensional transition metal dichalcogenide-based counter electrodes for dye-sensitized solar cells, RSC Adv. 7 (2017) 28234–28290, https://doi.org/10.1039/C7RA03599C.

[52] Y. Hu, X. Zhu, L. Wang, Two-dimensional material-functionalized separators for high-energy-density metal–sulfur and metal-based batteries, ChemSusChem. 13 (2020) 1366–1378, https://doi.org/10.1002/cssc.201902758.

[53] Y.V. Lim, X.L. Li, H.Y. Yang, Recent tactics and advances in the application of metal sulfides as high-performance anode materials for rechargeable sodium-ion batteries, Adv. Funct. Mater. 31 (2021) 2006761, https://doi.org/10.1002/adfm.202006761.

[54] C. Chandra, H.S. Cahyadi, S. Alvin, W. Devina, J.-H. Park, W. Chang, K.Y. Chung, S.K. Kwak, J. Kim, Revealing the sodium storage mechanism in high-temperature-synthesized silicon oxycarbides, Chem. Mater. 32 (2019) 410–423, https://doi.org/10.1021/acs.chemmater.9b04018.

[55] B. Xiao, F.A. Soto, M. Gu, K.S. Han, J. Song, H. Wang, M.H. Engelhard, V. Murugesan, K.T. Mueller, D. Reed, Lithium-pretreated hard carbon as high-performance sodium-ion battery anodes, Adv. Energy Mater. 8 (2018) 1801441, https://doi.org/10.1002/aenm.201801441.

[56] W. Li, S.L. Chou, J.Z. Wang, J.H. Kim, H.K. Liu, S.X. Dou, Sn$_4$+ xP$_3$@ amorphous Sn-P composites as anodes for sodium-ion batteries with low cost, high capacity, long life, and superior rate capability, Adv. Mater. 26 (2014) 4037–4042, https://doi.org/10.1002/adma.201400794.

[57] D. Puthusseri, M. Wahid, S. Ogale, Conversion-type anode materials for alkali-ion batteries: state of the art and possible research directions, ACS Omega 3 (2018) 4591–4601, https://doi.org/10.1021/acsomega.8b00188.

[58] Z. Li, H. Zhao, Recent developments of phosphorus-based anodes for sodium ion batteries, J. Mater. Chem. A 6 (2018) 24013–24030, https://doi.org/10.1039/C8TA08774A.

[59] H. Su, S. Jaffer, H. Yu, Transition metal oxides for sodium-ion batteries, Energy Storage Mater. 5 (2016) 116–131, https://doi.org/10.1016/j.ensm.2016.06.005.

[60] A. Bhat, S. Anwer, K.S. Bhat, M.I.H. Mohideen, K. Liao, A. Qurashi, Prospects challenges and stability of 2D MXenes for clean energy conversion and storage applications, NPJ 2D Mater. Appl. 5 (2021) 1–21, https://doi.org/10.1038/s41699-021-00239-8.

[61] J. Wang, Y.S. Li, P. Liu, F. Wang, Q.-R. Yao, Y.-J. Zou, H.-Y. Zhou, M. Balogun, J.-Q. Deng, Green large-scale production of N/O-dual doping hard carbon derived from bagasse as high-performance anodes for sodium-ion batteries, J. Cent. South Univ. 28 (2021) 361–369, https://doi.org/10.1007/s11771-021-4608-y.

[62] G. Wang, S. Wang, X. Sun, Y. Liu, P. Nie, L. Hou, L. Chang, C. Yuan, Metallic Mo$_2$C quantum dots confined in functional carbon nanofiber films toward efficient sodium storage: heterogeneous interface engineering and charge-storage mechanism, ACS Appl. Energy Mater. 5 (2021) 1114–1125, https://doi.org/10.1021/acsaem.1c03477.

[63] Y. Dong, S.S.K. Mallineni, K. Maleski, H. Behlow, V.N. Mochalin, A.M. Rao, Y. Gogotsi, R. Podila, Metallic MXenes: a new family of materials for flexible triboelectric nanogenerators, Nano Energy 44 (2018) 103–110, https://doi.org/10.1016/j.nanoen.2017.11.044.

[64] M.R. Lukatskaya, O. Mashtalir, C.E. Ren, Y. Dall'Agnese, P. Rozier, P.L. Taberna, M. Naguib, P. Simon, M.W. Barsoum, Y. Gogotsi, Cation intercalation and high volumetric capacitance of two-dimensional titanium carbide, Science 341 (2013) 1502–1505, https://doi.org/10.1126/science.1241488.

[65] A. Vahid Mohammadi, A. Hadjikhani, S. Shahbaz mohamadi, M. Beidaghi, Two-dimensional vanadium carbide (MXene) as a high-capacity cathode material for rechargeable aluminum batteries, ACS Nano 11 (2017) 11135–11144, https://doi.org/10.1021/acsnano.7b05350.

[66] Y. Xie, Y. Dall'Agnese, M. Naguib, Y. Gogotsi, M.W. Barsoum, H.L. Zhuang, P. R. Kent, Prediction and characterization of MXene nanosheet anodes for non-lithium-ion batteries, ACS Nano 8 (2014) 9606–9615, https://doi.org/10.1021/nn503921j.

[67] Y. Xie, M. Naguib, V.N. Mochalin, M.W. Barsoum, Y. Gogotsi, X. Yu, K.-W. Nam, X.-Q. Yang, A.I. Kolesnikov, P.R. Kent, Role of surface structure on Li-ion energy storage capacity of two-dimensional transition-metal carbides, J. Am. Chem. Soc. 136 (2014) 6385–6394, https://doi.org/10.1021/ja501520b.

[68] W. Bao, X. Tang, X. Guo, S. Choi, C. Wang, Y. Gogotsi, G. Wang, Porous cryo-dried MXene for efficient capacitive deionization, Joule 2 (2018) 778–787, https://doi.org/10.1016/j.joule.2018.02.018.

[69] F. Shahzad, M. Alhabeb, C.B. Hatter, B. Anasori, S. Man Hong, C.M. Koo, Y. Gogotsi, Electromagnetic interference shielding with 2D transition metal carbides (MXenes), Science 353 (2016) 1137–1140, https://doi.org/10.1126/science.aag2421.

[70] N. Qin, Y. Sun, C. Hu, S. Liu, Z. Luo, X. Cao, S. Liang, G. Fang, Boosting high initial coulombic efficiency of hard carbon by in-situ electrochemical presodiation, J. Energy Chem. 77 (2022) 310–316, https://doi.org/10.1016/j.jechem.2022.10.032.

[71] X. Sun, J. Zhang, Y. Wang, Y. Zhang, L. Hou, Y. Liu, C. Yuan, Self-assembly construction of hollow Ti$_3$C$_2$Tx Submicro-Tubes towards efficient alkali metal ion storage, J. Chem. Eng. 433 (2022), 134506, https://doi.org/10.1016/j.cej.2022.134506.

[72] X. Tang, X. Guo, W. Wu, G. Wang, 2D metal carbides and nitrides (MXenes) as high-performance electrode materials for Lithium-based batteries, Adv. Energy Mater. 8 (2018) 1801897, https://doi.org/10.1002/aenm.201801897.

[73] O. Folorunso, N. Kumar, Y. Hamam, R. Sadiku, S.S. Ray, Recent progress on 2D metal carbide/nitride (MXene) nanocomposites for lithium-based batteries, FlatChem. 29 (2021), 100281, https://doi.org/10.1016/j.flatc.2021.100281.

[74] C. Eames, M.S. Islam, Ion intercalation into two-dimensional transition-metal carbides: global screening for new high-capacity battery materials, J. Am. Chem. Soc. 136 (2014) 16270–16276, https://doi.org/10.1021/ja508154e.

[75] E. Yang, H. Ji, J. Kim, H. Kim, Y. Jung, Exploring the possibilities of two-dimensional transition metal carbides as anode materials for sodium batteries, Phys. Chem. Chem. Phys. 17 (2015) 5000–5005, https://doi.org/10.1039/C4CP05140H.

[76] J. Tang, X. Peng, T. Lin, X. Huang, B. Luo, L. Wang, Confining ultrafine tin monophosphide in Ti$_3$C$_2$Tx interlayers for rapid and stable sodium ion storage, Science 1 (2021) 203–211, https://doi.org/10.1016/j.esci.2021.12.004.

[77] S.Y. Hong, Y. Kim, Y. Park, A. Choi, N.-S. Choi, K.T. Lee, Charge carriers in rechargeable batteries: Na ions vs. Li ions, Energy Environ. Sci. 6 (2013) 2067–2081, https://doi.org/10.1039/C3EE40811F.

[78] L. Yu, L.P. Wang, H. Liao, J. Wang, Z. Feng, O. Lev, J.S. Loo, M.T. Sougrati, Z. J. Xu, Understanding fundamentals and reaction mechanisms of electrode materials for na-ion batteries, Small 14 (2018) 1703338, https://doi.org/10.1002/smll.201703338.

[79] H. Pan, Y.-S. Hu, L. Chen, Room-temperature stationary sodium-ion batteries for large-scale electric energy storage, Energy Environ. Sci. 6 (2013) 2338–2360, https://doi.org/10.1039/C3EE40847G.

[80] S.W. Kim, D.H. Seo, X. Ma, G. Ceder, K. Kang, Electrode materials for rechargeable sodium-ion batteries: potential alternatives to current lithium-ion batteries, Adv. Energy Mater. 2 (2012) 710–721, https://doi.org/10.1002/aenm.201200026.

[81] M. Jackle, A. Groß, Microscopic properties of lithium, sodium, and magnesium battery anode materials related to possible dendrite growth, J. Chem. Phys. 141 (2014), 174710, https://doi.org/10.1063/1.4901055.

[82] J.W. Choi, D. Aurbach, Promise and reality of post-lithium-ion batteries with high energy densities, Nat. Rev. Mater. 1 (2016) 1–16, https://doi.org/10.1038/natrevmats.2016.13.

[83] B.L. Ellis, L.F. Nazar, Sodium and sodium-ion energy storage batteries, Curr Opin Solid State Mater Sci. 16 (2012) 168–177, https://doi.org/10.1016/j.cossms.2012.04.002.

[84] S. Guo, J. Yi, Y. Sun, H. Zhou, Recent advances in titanium-based electrode materials for stationary sodium-ion batteries, Energy Environ. Sci. 9 (2016) 2978–3006, https://doi.org/10.1039/C6EE01807F.

[85] K.B. Hueso, M. Armand, T. Rojo, High temperature sodium batteries: status, challenges and future trends, Energy Environ. Sci. 6 (2013) 734–749, https://doi.org/10.1039/C3EE24086J.

[86] S.A. Delp, O. Borodin, M. Olguin, C.G. Eisner, J.L. Allen, T.R. Jow, Importance of reduction and oxidation stability of high voltage electrolytes and additives, Electrochim. Acta. 209 (2016) 498–510, https://doi.org/10.1016/j.electacta.2016.05.100.

[87] X. Zhang, Z. Zhang, S. Yao, A. Chen, X. Zhao, Z. Zhou, An effective method to screen sodium-based layered materials for sodium ion batteries, Npj Comput. Mater. 4 (2018) 1-6, 10.1038/s41524-018-0070-2.

[88] J. Hu, B. Xu, S.A. Yang, S. Guan, C. Ouyang, Y. Yao, 2D electrides as promising anode materials for Na-ion batteries from first-principles study, ACS Appl. Mater. Interfaces 7 (2015) 24016–24022, https://doi.org/10.1021/acsami.5b06847.

[89] J. Hou, K. Tu, Z. Chen, Two-dimensional Y2C electride: a promising anode material for Na-Ion batteries, J. Phys. Chem. C 120 (2016) 18473–18478, https://doi.org/10.1021/acs.jpcc.6b06087.

[90] Q. Meng, J. Ma, Y. Zhang, Z. Li, C. Zhi, A. Hu, J. Fan, The S-functionalized Ti3C2 Mxene as a high capacity electrode material for Na-ion batteries: a DFT study, Nanoscale. 10 (2018) 3385–3392, https://doi.org/10.1039/C7NR07649E.

[91] T.B. Kocabaş, A. Özden, I.L. Demiroğlu, D. Çakır, C. Sevik, Determination of dynamically stable electrenes toward ultrafast charging battery applications, J. Phys. Chem. Lett. Lett. 9 (2018) 4267–4274, https://doi.org/10.1021/acs.jpclett.8b01468.

[92] J. Zhu, D. Yang, Z. Yin, Q. Yan, H. Zhang, Graphene and graphene-based materials for energy storage applications, Small 10 (2014) 3480–3498, https://doi.org/10.1002/smll.201303202.

[93] H. Kim, K.-Y. Park, J. Hong, K. Kang, All-graphene-battery: bridging the gap between supercapacitors and lithium ion batteries, Sci. Rep. 4 (2014) 1–8, https://doi.org/10.1038/srep05278.

[94] C. Uthaisar, V. Barone, J.E. Peralta, Lithium adsorption on zigzag graphene nanoribbons, J. Appl. Phys. 106 (2009), 113715, https://doi.org/10.1063/1.3265431.

[95] L.J. Zhou, Z. Hou, L.M. Wu, First-principles study of lithium adsorption and diffusion on graphene with point defects, J. Phys. Chem. C 116 (2012) 21780–21787, https://doi.org/10.1021/jp304861d.

[96] D. Datta, J. Li, V.B. Shenoy, Defective graphene as a high-capacity anode material for Na-and Ca-ion batteries, ACS Appl. Mater. Interfaces 6 (2014) 1788–1795, https://doi.org/10.1021/am404788e.

[97] W. Ai, Z. Luo, J. Jiang, J. Zhu, Z. Du, Z. Fan, L. Xie, H. Zhang, W. Huang, T. Yu, Nitrogen and sulfur codoped graphene: multifunctional electrode materials for high-performance Li-ion batteries and oxygen reduction reaction, Adv. Mater. 26 (2014) 6186–6192, https://doi.org/10.1002/adma.201401427.

[98] A. Osadchy, E. Obraztsova, V. Savin, Y.P. Svirko, Computer simulation of edge-terminated carbon nanoribbons, Bull. Lebedev Phys. Inst. 44 (2017) 151–153, https://doi.org/10.3103/S1068335617050074.

[99] H. Zhang, M. Zhao, X. He, Z. Wang, X. Zhang, X. Liu, High mobility and high storage capacity of lithium in sp–sp2 hybridized carbon network: the case of graphyne, J. Phys. Chem. C 115 (2011) 8845–8850, https://doi.org/10.1021/jp201062m.

[100] J. Sun, G. Zheng, H.-W. Lee, N. Liu, H. Wang, H. Yao, W. Yang, Y. Cui, Formation of stable phosphorus–carbon bond for enhanced performance in black phosphorus nanoparticle–graphite composite battery anodes, Nano Lett. 14 (2014) 4573–4580, https://doi.org/10.1021/nl501617j.

[101] W. Li, Y. Yang, G. Zhang, Y.-W. Zhang, Ultrafast and directional diffusion of lithium in phosphorene for high-performance lithium-ion battery, Nano Lett. 15 (2015) 1691–1697, https://doi.org/10.1021/nl504336h.

[102] M. Batmunkh, M. Bat-Erdene, J.G. Shapter, Phosphorene and phosphorene-based materials–prospects for future applications, Adv. Mater. 28 (2016) 8586–8617, https://doi.org/10.1002/adma.201602254.

[103] J. Carrete, W. Li, L. Lindsay, D.A. Broido, L.J. Gallego, N. Mingo, Physically founded phonon dispersions of few-layer materials and the case of borophene, Mater. Res. Lett. 4 (2016) 204–211, https://doi.org/10.1080/21663831.2016.1174163.

[104] S. Cahangirov, M. Topsakal, E. Aktürk, H. Şahin, S. Ciraci, Two-and one-dimensional honeycomb structures of silicon and germanium, Phys. Rev. Lett. 102 (2009), 236804, https://doi.org/10.1103/PhysRevLett.102.236804.

[105] B. Singh, C.H. Hsu, W.F. Tsai, V.M. Pereira, H. Lin, Stable charge density wave phase in a 1 T-TiSe2 monolayer, Phys. Rev. B 95 (2017), 245136, https://doi.org/10.1103/PhysRevB.95.245136.

[106] A. Togo, I. Tanaka, First principles phonon calculations in materials science, Scr. Mater. 108 (2015) 1–5, https://doi.org/10.1016/j.scriptamat.2015.07.021.

[107] F. Mouhat, F.X. Coudert, Necessary and sufficient elastic stability conditions in various crystal systems, Phys. Rev. B 90 (2014), 224104, https://doi.org/10.1103/PhysRevB.90.224104.

[108] M.N. Blonsky, H.L. Zhuang, A.K. Singh, R.G. Hennig, Ab initio prediction of piezoelectricity in two-dimensional materials, ACS Nano 9 (2015) 9885–9891, https://doi.org/10.1021/acsnano.5b03394.

[109] J. Rehman, R. Ali, N. Ahmad, X. Lv, C. Guo, Theoretical investigation of strain-engineered WSe2 monolayers as anode material for Li-ion batteries, J. Alloys Compd. 804 (2019) 370–375, https://doi.org/10.1016/j.jallcom.2019.07.040.

[110] Z. Shunhong, Z. Jian, W. Qian, C. Xiaoshuang, K. Yoshiyuki, J. Puru, Penta-graphene: a new carbon allotrope, Proc. Natl. Acad. Sci. 7 (2015) 191–207, https://doi.org/10.1073/pnas.1416591112.

[111] D. Wang, L.M. Liu, S.J. Zhao, Z.Y. Hu, H. Liu, Potential application of metal dichalcogenides double-layered heterostructures as anode materials for Li-ion batteries, The, J. Phys. Chem. C 120 (2016) 4779–4788, https://doi.org/10.1021/acs.jpcc.5b11677.

[112] T. Yu, Z. Zhao, L. Liu, S. Zhang, H. Xu, G. Yang, TiC3 monolayer with high specific capacity for sodium-ion batteries, J. Am. Chem. Soc. 140 (2018) 5962–5968, https://doi.org/10.1021/jacs.8b02016.

[113] S. Fan, X. Zou, H. Du, L. Gan, C. Xu, W. Lv, Y.-B. He, Q.H. Yang, F. Kang, J. Li, Theoretical investigation of the intercalation chemistry of lithium/sodium ions in transition metal dichalcogenides, J. Phys. Chem. C 121 (2017) 13599–13605, https://doi.org/10.1021/acs.jpcc.7b05303.

[114] J. Rehman, X. Fan, M. Butt, A. Laref, V.A. Dinh, W. Zheng, First principles predictions of Na and K storage in layered SnSe2, Appl. Surf. Sci. 566 (2021), 150522, https://doi.org/10.1016/j.apsusc.2021.150522.

[115] M. Mortazavi, C. Wang, J. Deng, V.B. Shenoy, N.V. Medhekar, Ab initio characterization of layered MoS2 as anode for sodium-ion batteries, J. Power Sources. 268 (2014) 279–286, https://doi.org/10.1016/j.jpowsour.2014.06.049.

[116] S. Zhang, T. Jow, Study of poly (acrylonitrile-methyl methacrylate) as binder for graphite anode and LiMn2O4 cathode of Li-ion batteries, J. Power Sources. 109 (2002) 422–426, https://doi.org/10.1016/S0378-7753(02)00107-6.

[117] H. Zheng, K. Jiang, T. Abe, Z. Ogumi, Electrochemical intercalation of lithium into a natural graphite anode in quaternary ammonium-based ionic liquid electrolytes, Carbon. 44 (2006) 203–210, https://doi.org/10.1016/j.carbon.2005.07.038.

[118] Z. Yang, D. Choi, S. Kerisit, K.M. Rosso, D. Wang, J. Zhang, G. Graff, J. Liu, Nanostructures and lithium electrochemical reactivity of lithium titanites and titanium oxides: A review, J. Power Sources. 192 (2009) 588–598, https://doi.org/10.1016/j.jpowsour.2009.02.038.

[119] Z. Deng, Y. Mo, S.P. Ong, Computational studies of solid-state alkali conduction in rechargeable alkali-ion batteries, NPG Asia Mater. 8 (2016) e254–e, https://doi.org/10.1038/am.2016.7.

[120] G. Mills, H. Jónsson, G.K. Schenter, Reversible work transition state theory: application to dissociative adsorption of hydrogen, Surf Sci. 324 (1995) 305–337, https://doi.org/10.1016/0039-6028(94)00731-4.

[121] G. Henkelman, B.P. Uberuaga, H. Jónsson, A climbing image nudged elastic band method for finding saddle points and minimum energy paths, J. Chem. Phys. 113 (2000) 9901–9904, https://doi.org/10.1063/1.1329672.

[122] Y. Mo, S.P. Ong, G. Ceder, Insights into diffusion mechanisms in P2 layered oxide materials by first-principles calculations, Chem. Mater. 26 (2014) 5208–5214, https://doi.org/10.1021/cm501563f.

[123] A. Urban, D.-H. Seo, G. Ceder, Computational understanding of Li-ion batteries, Npj Comput. Mater. 2 (2016) 1–13, https://doi.org/10.1038/npjcompumats.2016.2.

[124] Q. Bai, L. Yang, H. Chen, Y. Mo, Computational studies of electrode materials in sodium-ion batteries, Adv. Energy Mater. 8 (2018) 1702998, https://doi.org/10.1002/aenm.201702998.

[125] S.P. Ong, V.L. Chevrier, G. Hautier, A. Jain, C. Moore, S. Kim, X. Ma, G. Ceder, Voltage, stability and diffusion barrier differences between sodium-ion and lithium-ion intercalation materials, Energy Environ. Sci. 4 (2011) 3680–3688, https://doi.org/10.1039/C1EE01782A.

[126] C. Zheng, B. Radhakrishnan, I.H. Chu, Z. Wang, S.P. Ong, Effects of transition-metal mixing on Na ordering and kinetics in layered P2 oxides, Phys. Rev. Appl. 7 (2017), 064003, https://doi.org/10.1103/physrevapplied.7.064003.

[127] X. Han, C. Liu, J. Sun, A.D. Sendek, W. Yang, Density functional theory calculations for evaluation of phosphorene as a potential anode material for magnesium batteries, RSC Adv. 8 (2018) 7196–7204, https://doi.org/10.1039/C7RA12400G.

[128] J. Zhao, Y. Zhang, Y. Wang, H. Li, Y. Peng, The application of nanostructured transition metal sulfides as anodes for lithium ion batteries, J. Energy Chem. 27 (2018) 1536–1554, https://doi.org/10.1016/j.jechem.2018.01.009.

[129] B. Mendoza-Sánchez, Y. Gogotsi, Synthesis of two-dimensional materials for capacitive energy storage, Adv. Mater. 28 (2016) 6104–6135, https://doi.org/10.1002/adma.201506133.

[130] Z. Wei, L. Wang, M. Zhuo, W. Ni, H. Wang, J. Ma, Layered tin sulfide and selenide anode materials for Li-and Na-ion batteries, J. Mater. Chem. A. 6 (2018) 12185–12214, https://doi.org/10.1039/C8TA02695E.

[131] L. Wang, J. Wang, F. Guo, L. Ma, Y. Ren, T. Wu, P. Zuo, G. Yin, J. Wang, Understanding the initial irreversibility of metal sulfides for sodium-ion batteries via operando techniques, Nano Energy. 43 (2018) 184–191, https://doi.org/10.1016/j.nanoen.2017.11.029.

[132] Y. Liu, Y. Fang, Z. Zhao, C. Yuan, X.W. Lou, A ternary Fe1−xS@ porous carbon nanowires/reduced graphene oxide hybrid film electrode with superior volumetric and gravimetric capacities for flexible sodium ion batteries, Adv. Energy Mater. 9 (2019) 1803052, https://doi.org/10.1002/aenm.201803052.

[133] Y. Zhao, L.P. Wang, M.T. Sougrati, Z. Feng, Y. Leconte, A. Fisher, M. Srinivasan, Z. Xu, A review on design strategies for carbon based metal oxides and sulfides nanocomposites for high performance Li and Na ion battery anodes, Adv. Energy Mater. 7 (2017) 1601424, https://doi.org/10.1002/aenm.201601424.

[134] G. Li, D. Luo, X. Wang, M.H. Seo, S. Hemmati, A. Yu, Z. Chen, Enhanced reversible sodium-ion intercalation by synergistic coupling of few-layered MoS2 and S-doped graphene, Adv. Funct. Mater. 27 (2017) 1702562, https://doi.org/10.1002/adfm.201702562.

[135] Y. Zhang, P. Zhu, L. Huang, J. Xie, S. Zhang, G. Cao, X. Zhao, Few-layered SnS2 on few-layered reduced graphene oxide as Na-ion battery anode with ultralong cycle life and superior rate capability, Adv. Funct. Mater. 25 (2015) 481–489, https://doi.org/10.1002/adfm.201402833.

[136] R. Sun, Q. Wei, Q. Li, W. Luo, Q. An, J. Sheng, D. Wang, W. Chen, L. Mai, Vanadium sulfide on reduced graphene oxide layer as a promising anode for sodium ion battery, ACS Appl. Mater. Interfaces. 7 (2015) 20902–20908, https://doi.org/10.1021/acsami.5b06385.

[137] T. Lei, W. Chen, J. Huang, C. Yan, H. Sun, C. Wang, W. Zhang, Y. Li, J. Xiong, Multi-functional layered WS2 nanosheets for enhancing the performance of lithium–sulfur batteries, Adv. Energy Mater. 7 (2017) 1601843, https://doi.org/10.1002/aenm.201601843.

[138] Z. Sun, Y. Liu, D. Wu, K. Tan, L. Hou, C. Yuan, Construction of a multi-dimensional flexible MnS based paper electrode with ultra-stable and high-rate capability towards efficient sodium storage, Nanoscale. 12 (2020) 4119–4127, https://doi.org/10.1039/C9NR09903D.

[139] M.A. McGuire, Crystal and magnetic structures in layered, transition metal dihalides and trihalides, Crystals. 7 (2017) 121, 10.4850/arXiv.1704.0822.

[140] D. Wang, Y. Liu, X. Meng, Y. Wei, Y. Zhao, G. Pang, G. Chen, Two-dimensional VS2 monolayers as potential anode materials for lithium-ion batteries and beyond: first-principles calculations, J. Mater. Chem. A 5 (2017) 21370–21377, https://doi.org/10.1039/C7TA06944H.

[141] D.B. Putungan, S.-H. Lin, J.-L. Kuo, Metallic VS2 monolayer polytypes as potential sodium-ion battery anode via ab initio random structure searching, ACS Appl. Mater. Interfaces 8 (2016) 18754–18762, https://doi.org/10.1021/acsami.6b03499.

[142] J. Feng, X. Sun, C. Wu, L. Peng, C. Lin, S. Hu, J. Yang, Y. Xie, Metallic few-layered VS2 ultrathin nanosheets: high two-dimensional conductivity for in-plane supercapacitors, J. Am. Chem. Soc. 133 (2011) 17832–17838, https://doi.org/10.1021/ja207176c.

[143] L. Cai, Q. Zhang, J.P. Mwizerwa, H. Wan, X. Yang, X. Xu, X. Yao, Highly crystalline layered VS2 nanosheets for all-solid-state lithium batteries with enhanced electrochemical performances, ACS Appl. Mater. Interfaces 10 (2018) 10053–10063, https://doi.org/10.1021/acsami.7b18798.

[144] R. Sun, Q. Wei, J. Sheng, C. Shi, Q. An, S. Liu, L. Mai, Novel layer-by-layer stacked VS2 nanosheets with intercalation pseudocapacitance for high-rate sodium ion charge storage, Nano Energy 35 (2017) 396–404, https://doi.org/10.1016/j.nanoen.2017.03.036.

[145] Y.-M. Chang, H.-W. Lin, L.-J. Li, H.-Y. Chen, Two-dimensional materials as anodes for sodium-ion batteries, Mater. Today Adv. 6 (2020), 100054, https://doi.org/10.1016/j.mtadv.2020.100054.

[146] A. Samad, A. Shafique, Y.-H. Shin, Adsorption and diffusion of mono, di, and trivalent ions on two-dimensional TiS2, Nanotechnology. 28 (2017), 175401, https://doi.org/10.1088/1361-6528/aa6536.

[147] J. Tang, X. Huang, T. Lin, T. Qiu, H. Huang, X. Zhu, Q. Gu, B. Luo, L. Wang, MXene derived TiS2 nanosheets for high-rate and long-life sodium-ion capacitors, Energy Storage Mater. 26 (2020) 550–559, https://doi.org/10.1016/j.ensm.2019.11.028.

[148] A. Chaturvedi, E. Edison, N. Arun, P. Hu, C. Kloc, V. Aravindan, S. Madhavi, Two dimensional TiS2 as a promising insertion anode for na-ion battery, ChemistrySelect 3 (2018) 524–528, https://doi.org/10.1002/slct.201702181.

[149] J. Su, Y. Pei, Z. Yang, X. Wang, Ab initio study of graphene-like monolayer molybdenum disulfide as a promising anode material for rechargeable sodium ion batteries, RSC Adv. 4 (2014) 43183–43188, https://doi.org/10.1039/C4RA06557C.

[150] D. Su, S. Dou, G. Wang, Ultrathin MoS2 nanosheets as anode materials for sodium-ion batteries with superior performance, Adv. Energy Mater. 5 (2015) 1401205, https://doi.org/10.1002/aenm.201401205.

[151] S.-K. Park, J. Lee, S. Bong, B. Jang, K.-D. Seong, Y. Piao, Scalable synthesis of few-layer MoS2 incorporated into hierarchical porous carbon nanosheets for high-performance Li-and Na-ion battery anodes, ACS Appl. Mater. Interfaces 8 (2016) 19456–19465, https://doi.org/10.1021/acsami.6b05010.

[152] F. Li, Y. Qu, M. Zhao, Germanium sulfide nanosheet: a universal anode material for alkali metal ion batteries, J. Mater. Chem A 4 (2016) 8905–8912, https://doi.org/10.1039/C6TA03210A.

[153] C.C. Li, B. Wang, D. Chen, L.-Y. Gan, Y. Feng, Y. Zhang, Y. Yang, H. Geng, X. Rui, Y. Yu, Topotactic transformation synthesis of 2D ultrathin GeS2 nanosheets toward high-rate and high-energy-density sodium-ion half/full batteries, ACS nano. 14 (2019) 531–540, https://doi.org/10.1021/acsnano.9b06855.

[154] B. Wang, W. Du, Y. Yang, Y. Zhang, Q. Zhang, X. Rui, H. Geng, C.C. Li, Two-Dimensional germanium sulfide nanosheets as an ultra-stable and high capacity anode for lithium ion batteries, Chem. Eur. J. 26 (2020) 6554–6560, https://doi.org/10.1002/chem.201904116.

[155] A. Samad, M. Noor-A-Alam, Y.-H. Shin, First principles study of a SnS2/graphene heterostructure: a promising anode material for rechargeable Na ion batteries, J. Mater. Chem A 4 (2016) 14316–14323, https://doi.org/10.1039/C6TA05739J.

[156] R. Thangavel, A. Samuthira Pandian, H.V. Ramasamy, Y.S. Lee, Rapidly synthesized, few-layered pseudocapacitive SnS2 anode for high-power sodium ion batteries, ACS Appl. Mater. Interfaces. 9 (2017) 40187–40196, https://doi.org/10.1021/acsami.7b11040.

[157] T. Zhou, W.K. Pang, C. Zhang, J. Yang, Z. Chen, H.K. Liu, Z. Guo, Enhanced sodium-ion battery performance by structural phase transition from two-dimensional hexagonal-SnS2 to orthorhombic-SnS, Acs Nano 8 (2014) 8323–8333, https://doi.org/10.1021/nn503582c.

[158] H. Jiang, T. Zhao, Y. Ren, R. Zhang, M. Wu, Ab initio prediction and characterization of phosphorene-like SiS and SiSe as anode materials for sodium-ion batteries, Sci. Bull. 62 (2017) 572–578, https://doi.org/10.1016/j.scib.2017.03.026.

[159] T.D. Pham, H.D. Luong, K. Sato, Y. Shibutani, V.A. Dinh, Two-dimensional Na x SiS as a promising anode material for rechargeable sodium-based batteries: ab

[160] Y. Guo, T. Bo, Y. Wu, J. Zhang, Z. Lu, W. Li, X. Li, P. Zhang, B. Wang, YS2 monolayer as a high-efficient anode material for rechargeable Li-ion and Na-ion batteries, Solid State Ion 345 (2020), 115187, https://doi.org/10.1016/j.ssi.2019.115187.

[161] W. Mao, Y. Ding, M. Li, C. Ma, H. Gong, J. Pan, S. Zhang, Y. Qian, K. Bao, Synthesis and electrochemical characterization of 2D SnS2/RGO as anode material in sodium-ion batteries, J. Alloys Compd. 855 (2021), 157209, https://doi.org/10.1016/j.jallcom.2020.157209.

[162] D. Zhou, C. Li, F. Yin, X. Tang, C. Pu, C. He, Two-dimensional 1T-PS2 as a promising anode material for sodium-ion batteries with ultra-high capacity, low average voltage and appropriate mobility, Chin. Chem. Lett. 31 (2020) 2325–2329, https://doi.org/10.1016/j.cclet.2020.04.045.

[163] S. Lei, X. Chen, B. Xiao, W. Zhang, J. Liu, Excellent electrolyte wettability and high energy density of B2S as a two-dimensional Dirac anode for non-lithium-ion batteries, ACS Appl. Mater. Interfaces, 11 (2019) 28830-28840, 10.1021/acsami.9b07219.

[164] P. Li, Z. Li, J. Yang, Rational design of two-dimensional anode materials: B2S as a strained graphene, J. Phys. Chem. Lett. 9 (2018) 4852–4856, https://doi.org/10.1021/acs.jpclett.8b02035.

[165] E. Yang, H. Ji, Y. Jung, Two-dimensional transition metal dichalcogenide monolayers as promising sodium ion battery anodes, J. Phys. Chem. C. 119 (2015) 26374–26380, https://doi.org/10.1021/acs.jpcc.5b09935.

[166] X. Ou, X. Xiong, F. Zheng, C. Yang, Z. Lin, R. Hu, C. Jin, Y. Chen, M. Liu, In situ X-ray diffraction characterization of NbS2 nanosheets as the anode material for sodium ion batteries, J. Power Sources. 325 (2016) 410–416, https://doi.org/10.1016/j.jpowsour.2016.06.055.

[167] S. Kim, Y.J. Kim, W.-H. Ryu, Zirconium disulfides as an electrode material alternative for Li-ion batteries, Appl. Surf. Sci. 547 (2021), 149029, https://doi.org/10.1016/j.apsusc.2021.149029.

[168] M. Debbichi, A. Mallah, M.H. Dhaou, S. Lebègue, First-Principles Study of Monolayer pe nta-CoS2 as a Promising Anode Material for Li/Na-ion Batteries, Phys. Rev. Appl. 16 (2021), 024016, https://doi.org/10.1063/1.5110225.

[169] G.R. Vakili-Nezhaad, M. Al-Wadhahi, A.M. Gujrathi, N. Al-Rawahi, M. Mohammadi, Exploring the possibility of the zigzag WS2 nanoribbons as anode materials for sodium-ion batteries, Appl. Phys. A. 125 (2019) 1–8, https://doi.org/10.1007/s00339-018-2336-4.

[170] D. Zhoua, C. Li, F. Yin, X. Tang, C. Pu, C. He, Pua, Two-dimensional 1T-PS2 as a promising anode material for sodium-ion batteries with ultra-high capacity, low average voltage and appropriate mobility, Chin Chem Lett. 31 (2020) 2325–2329, https://doi.org/10.1016/j.cclet.2020.04.045.

[171] S. Lu, W. Hu, X. Hu, CuS2 sheets: a hidden anode material with a high capacity for sodium-ion batteries, J. Mater. Chem. C 9 (2021) 1387–1395, https://doi.org/10.1039/D0TC04946H.

[172] Y.-M. Li, Y.-L. Guo, Z.-Y. Jiao, The effect of S-functionalized and vacancies on V2C MXenes as anode materials for Na-ion and Li-ion batteries, Curr. Appl. Phys. 20 (2020) 310–319, https://doi.org/10.1016/j.cap.2019.11.025.

[173] F. Liu, J. Zhou, S. Wang, B. Wang, C. Shen, L. Wang, Q. Hu, Q. Huang, A. Zhou, Preparation of high-purity V2C MXene and electrochemical properties as Li-ion batteries, J. Electrochem. Soc. 164 (2017) A709, https://doi.org/10.1149/2.0641704jes.

[174] D. Er, J. Li, M. Naguib, Y. Gogotsi, V.B. Shenoy, Ti3C2 MXene as a high capacity electrode material for metal (Li, Na, K, Ca) ion batteries, ACS Appl. Mater. Interfaces 6 (2014) 11173–11179, https://doi.org/10.1021/am501144q.

[175] O. Mashtalir, M. Naguib, V.N. Mochalin, Y. Dall'Agnese, M. Heon, M.W. Barsoum, Y. Gogotsi,, Intercalation and delamination of layered carbides and carbonitrides, Nat. Commun. 4 (2013) 1–7, https://doi.org/10.1038/ncomms2664.

[176] S. Qi, F. Li, J. Wang, Y. Qu, Y. Yang, W. Li, M. Zhao, Prediction of a flexible anode material for Li/Na ion batteries: Phosphorous carbide monolayer (α-PC), Carbon. 141 (2019) 444–450, https://doi.org/10.1016/j.carbon.2018.09.031.

[177] X. Wang, S. Kajiyama, H. Iinuma, E. Hosono, S. Oro, I. Moriguchi, M. Okubo, A. Yamada, Pseudocapacitance of MXene nanosheets for high-power sodium-ion hybrid capacitors, Nat. Commun. 6 (2015) 1–6, https://doi.org/10.1038/ncomms7544.

[178] Y. Yu, Z. Guo, Q. Peng, J. Zhou, Z. Sun, Novel two-dimensional molybdenum carbides as high capacity anodes for lithium/sodium-ion batteries, J. Mater. Chem. A. 7 (2019) 12145–12153, https://doi.org/10.1039/C9TA02650A.

[179] X. Lv, J. Song, Y. Lai, J. Fang, J. Li, Z. Zhang, Ultrafine nanoparticles assembled Mo2C nanoplates as promising anode materials for sodium ion batteries with excellent performance, J. Energy Storage. 8 (2016) 205–211, https://doi.org/10.1016/j.est.2016.08.009.

[180] A. Samad, A. Shafique, H.J. Kim, Y.-H. Shin, Superionic and electronic conductivity in monolayer W2C:ab initio predictions, J. Mater. Chem. A. 5 (2017) 11094–11099, https://doi.org/10.1039/C7TA01177F.

[181] R.J. Baierle, C.J. Rupp, J. Anversa, Alkali (Li, K and Na) and alkali-earth (Be, Ca and Mg) adatoms on SiC single layer, Appl. Surf. Sci. 435 (2018) 338–345, https://doi.org/10.1016/j.apsusc.2017.11.068.

[182] A. Hosseinian, E.S. Khosroshahi, K. Nejati, E. Edjlali, E. Vessally, A DFT study on graphene, SiC, BN, and AlN nanosheets as anodes in Na-ion batteries, J. Mol. Model. 23 (2017) 1–7, https://doi.org/10.1007/s00894-017-3527-1.

[183] Y. Wang, Y. Li, Ab initio prediction of two-dimensional Si3C enabling high specific capacity as an anode material for Li/Na/K-ion batteries, J. Mater. Chem. A. 8 (2020) 4274–4282, https://doi.org/10.1039/C9TA11589G.

[184] T.S.D. Kumari, D. Jeyakumar, T.P. Kumar, Nano silicon carbide: a new lithium-insertion anode material on the horizon, RSC Adv. 3 (2013) 15028–15034, https://doi.org/10.1039/C3RA40798E.

[185] M.K. Butt, H.M. Zeeshan, V.A. Dinh, Y. Zhao, S. Wang, K. Jin, Monolayer SnC as anode material for Na ion batteries, Comput. Mater. Sci. 197 (2021), 110617, https://doi.org/10.1016/j.commatsci.2021.110617.

[186] H. Huang, H.H. Wu, C. Chi, B. Huang, T.Y. Zhang, Ab initio investigations of orthogonal ScC$_2$ and ScN$_2$ monolayers as promising anode materials for sodium-ion batteries, J. Mater. Chem. A 7 (2019) 8897–8904, https://doi.org/10.1039/C9TA00832B.

[187] X. Lv, W. Wei, Q. Sun, L. Yu, B. Huang, Y. Dai, Sc$_2$C as a promising anode material with high mobility and capacity: a first-principles study, ChemPhysChem 18 (2017) 1627–1634, https://doi.org/10.1002/cphc.201700181.

[188] C. Zhu, X. Qu, M. Zhang, J. Wang, Q. Li, Y. Geng, Y. Ma, Z. Su, Planar NiC$_3$ as a reversible anode material with high storage capacity for lithium-ion and sodium-ion batteries, J. Mater. Chem. A 7 (2019) 13356–13363, https://doi.org/10.1039/C9TA03494C.

[189] J. Hu, B. Xu, C. Ouyang, Y. Zhang, S.A. Yang, Investigations on Nb$_2$C monolayer as promising anode material for Li or non-Li ion batteries from first-principles calculations, RSC Adv. 6 (2016) 27467–27474, https://doi.org/10.1039/C5RA25028E.

[190] J. Zhao, J. Wen, L. Bai, J. Xiao, R. Zheng, X. Shan, L. Li, H. Gao, X. Zhang, One-step synthesis of few-layer niobium carbide MXene as a promising anode material for high-rate lithium ion batteries, Dalton trans. 48 (2019) 14433–14439, https://doi.org/10.1039/C9DT03260F.

[191] M. Naguib, J. Halim, J. Lu, K.M. Cook, L. Hultman, Y. Gogotsi, M.W. Barsoum, New two-dimensional niobium and vanadium carbides as promising materials for Li-ion batteries, J. Am. Chem. Soc. 135 (2013) 15966–15969, https://doi.org/10.1021/ja405735d.

[192] S. Wang, L. Shao, L. Yu, J. Guan, X. Shi, Z. Sun, J. Cai, H. Huang, A. Trukhanov, Niobium Carbide as a Promising Pseudocapacitive Sodium-Ion Storage Anode, Energy Technol. 9 (2021) 2100298, https://doi.org/10.1002/ente.202100298.

[193] K. Sheng, Z.Y. Wang, H.-K. Yuan, H. Chen, Two-dimensional hexagonal manganese carbide monolayer with intrinsic ferromagnetism and half-metallicity, New J. Phys. 22 (2020), 103049, https://doi.org/10.1088/1367-2630/abbf6c.

[194] Q. Chen, H. Wang, H. Li, Q. Duan, D. Jiang, J. Hou, Two-dimensional MnC as a potential anode material for Na/K-ion batteries: a theoretical study, J. Mol. Model. 26 (2020) 1–6, https://doi.org/10.1007/s00894-020-4326-7.

[195] N. Khossossi, A. Banerjee, I. Essaoudi, A. Ainane, P. Jena, R. Ahuja, Thermodynamics and kinetics of 2D g-GeC monolayer as an anode materials for Li/Na-ion batteries, J. Power Sources 485 (2021), 229318, https://doi.org/10.1016/j.jpowsour.2020.229318.

[196] S.-H. Zhang, B.-G. Liu, Superior ionic and electronic properties of ReN$_2$ monolayers for Na-ion battery electrodes, Nanotechnology 29 (2018), 325401, https://doi.org/10.1088/1361-6528/aac73b.

[197] F. Zhang, T. Jing, S. Cai, M. Deng, D. Liang, X. Qi, Two-dimensional ZrC$_2$ as a novel anode material with high capacity for sodium ion battery, Phys. Chem. Chem. Phys. 23 (2021) 12731–12738, https://doi.org/10.1039/D1CP00050K.

[198] Z. Zhao, T. Yu, S. Zhang, H. Xu, G. Yang, Y. Liu, Metallic P$_3$C monolayer as anode for sodium-ion batteries, J. Mater. Chem. A. 7 (2019) 405–411, https://doi.org/10.1039/C8TA09155B.

[199] Y. Wang, Y. Li, Two-dimensional Si$_3$C enables high specific capacity as promising novel anode material for Li/Na/K-ion batteries, J. Mater. Chem. A. 8 (2020) 4274–4282, https://doi.org/10.1039/C9TA11589G.

[200] K. H. Seng, M. H Park, Z. P. Guo, H. K. Liu, J. Cho, Self-assembled germanium/carbon nanostructures as high-power anode material for the lithium-ion battery, Angew. Chem. 124 (2012) 5755-5759.

[201] M. Wu, Y. He, L. Wang, Q. Xia, A. Zhou, Synthesis and electrochemical properties of V$_2$C MXene by etching in opened/closed environments, J. Adv. Ceram. 9 (2020) 749–758.